Sensors & Actuators: B. Chemical 394 (2023) 134359

Contents lists available at ScienceDirect

Sensors and Actuators: B. Chemical

journal homepage: www.elsevier.com/locate/snb

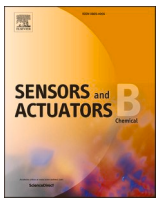

Highly sensitive and selective detection of benzene, toluene, xylene, and formaldehyde using Au-coated SnO_2 nanorod arrays for indoor air quality monitoring

Jihyun Lee [a,1], Hyegi Min [b,1], Yong-Sahm Choe [c], Yun Gyu Lee [d], Kichul Kim [d,*], Hyun-Sook Lee [a,*], Wooyoung Lee [a,*]

[a] Department of Materials Science and Engineering, Yonsei University, Seoul 03722, Republic of Korea
[b] KIURI Institute, Yonsei University, Seoul 03722, Republic of Korea
[c] Isenlab Inc., Halla Sigma Valley, Seongnam-si, Gyeonggi-do 13215, Republic of Korea
[d] Department of Building Research, Korea Institute of Civil Engineering and Building Technology, Goyang-Si 10223, Republic of Korea

ARTICLE INFO

Keywords:
Gas sensor
SnO_2 nanorod
Au catalyst
BTX
Formaldehyde
Gas chromatography

ABSTRACT

We report the high performance of Au-coated SnO_2 nanorod gas sensors for the detection of hazardous indoor volatile organic compounds (VOCs), such as benzene, toluene, xylene, and formaldehyde (BTXF) gases. Densely ordered SnO_2 nanorod arrays were prepared via glancing angle deposition with an electron beam evaporator. The Au layer coating was used as a heterogeneous catalyst to promote the oxidation of VOCs, such as hydrocarbons. After optimizing the Au thickness, the sensor exhibited an excellent sensing response and a rapid response time of < 2.5 s for 10 ppm of BTXF gases. The maximum response was ~662 for formaldehyde at 400 °C, ~328 for toluene at 450 °C, ~170 for xylene at 400 °C, and ~139 for benzene at 500 °C, which are significantly higher than those of previously reported metal-oxide-semiconductor-based sensors. Each gas was selectively detected by integrating the sensor into a miniaturized gas chromatography (GC) system. The sensors detected ppb-level gas concentrations. Significantly, GC analysis revealed that four types of gases could be separately detected in a mixed gas within 5 min. Our study shows that Au-coated SnO_2 nanorod gas sensors integrated with GC can be used as a facile indoor pollutant monitoring system.

1. Introduction

Most people spend majority of their days in various indoor spaces, such as homes, offices, stores, and vehicles. Indoor activities have recently been increasing owing to the high concentrations of external fine dust and occurrence of viral infections. Various hazardous volatile organic compounds (VOCs) are emitted from indoor building materials and household goods as gases. Therefore, monitoring indoor air pollution caused by VOCs has emerged as an important issue [1]. The presence of benzene, toluene, xylene, and formaldehyde (BTXF) is of major concern, even in low concentrations, because they can cause severe damage to the human body when exposed for a prolonged period, causing irritation, headaches, nausea, fatigue, dizziness, allergic reactions, and possibly cancer [2–4]. In addition, because the source of each BTXF is different, the degree of indoor air pollution caused by each BTXF gas varies from place to place. High-performance air monitoring systems can prevent these issues by detecting infinitesimal atmospheric BTXF content in real time [5]. However, most existing commercially available real-time air quality measuring devices detect temperature, humidity, fine dust, CO_2, CO, and total VOC contents but have the disadvantage of poor precision in measuring low concentrations of each VOC. Therefore, advanced detection techniques are required to sensitively and selectively detect indoor BTXF.

For several decades, quantitative and qualitative analysis techniques for gaseous compounds have been developed based on gas/liquid chromatographic methods combined with mass spectrometry (MS), photoionization detection (PID), and flame ionization detection (FID) [6]. These techniques can accurately detect infinitesimal concentrations of gas compounds, identify molecular species, and quantify them. However, these approaches are commercially limited owing to high

* Corresponding authors.
E-mail addresses: kichulkim@kict.re.kr (K. Kim), h-slee@yonsei.ac.kr (H.-S. Lee), wooyoung@yonsei.ac.kr (W. Lee).
[1] These authors contributed equally.

https://doi.org/10.1016/j.snb.2023.134359
Received 9 May 2023; Received in revised form 18 July 2023; Accepted 25 July 2023
Available online 27 July 2023

manufacturing and set-up expenses, inconvenient portability, and the need for scientific knowledge to operate. Metal oxide semiconductor (MOS) chemiresistors are promising gas analysis devices owing to their low manufacturing costs, compact sizes, and high portability. These sensors can sensitively detect target gaseous molecules, benefitting from their wide range of energy bandgap energies [7]. For MOS gas sensors, reducible metal oxide compounds have been used because the reduced state, termed an oxygen vacancy, promotes the ionization of atmospheric oxygen [8,9]. These ionized oxygen atoms participate as active sites in the oxidation reaction of the target molecules [7]. Electron transfer resulting from the chemical reaction causes a significant change in the resistance of the oxides, which can be easily recorded using conventional measurement techniques [9]. Herein, sensing materials have been modified in various ways to enhance gas sensing performance, such as increasing the surface area by controlling morphology [10–13], tuning the energy level by p/n junction formation [14–17], and introducing a large number of oxygen vacancies through heteroatom doping [18,19] or surface defect engineering [20,21]. These approaches confirm the enhanced sensitivity of gas sensors [22]. For instance, microtube-structured SnO_2 has been reported as a sensor material for formaldehyde gas, with a low detection limit of 10 ppb [13]. SnO/SnO_2 composites, which are heterojunctions between different oxidation states, exhibited superior formaldehyde sensing performance compared to homogenous SnO_2 gas sensors [15]. Furthermore, compared to pristine SnO_2 nanoparticles, SnO_2 with Ni doping introduced a high density of oxygen vacancies and showed 10 times higher sensing enhancement for formaldehyde gas [19]. These results demonstrate that MOS-based gas sensors are potential air monitoring systems that can be used to tune the structure of oxide compounds. However, despite the outstanding performance of conventional approaches, sensing selectivity to interfering gases and high-power consumption remain the main challenges of MOS gas sensors [23].

The use of noble metal-based catalysts is a facile approach to address these challenges by providing effective reaction pathways. Many catalytic studies have shown that noble metals (Au, Pt, and Pd) anchored on oxide surfaces act as heterogeneous catalysts, fostering the total combustion reaction of hydrocarbon molecules [24–27]. Previous density functional theory (DFT) calculations revealed that noble metals supported on the oxide surface promote the formation of oxygen vacancies by reducing the energy required to form vacancies at the perimeter sites of metal clusters [28]. In the chemical reaction, the vacancy sites can provide thermodynamically effective pathways; therefore, the reactions can occur at lower temperatures, simultaneously enhancing the molecular conversion rates. Several studies have shown that Au-based heterogeneous catalysts are suitable for effective VOC combustion reactions [29]. The gas-sensing mechanism is similar to that of a catalytic combustion reaction; hence, several gas sensors, such as Au/ZnO porous octahedrons [30] and Au-loaded MoO_3 hollow spheres [31], have also demonstrated outstanding gas-sensing performances for VOC gases. Therefore, heterogeneous catalytic reactions provide critical insights to improve gas sensing.

In this study, we investigated the sensing performance of Au-coated SnO_2 nanorod (NR) gas sensors for detecting hazardous indoor VOCs, such as BTXF gases. Rod-type SnO_2 with a high surface area and mechanical robustness was synthesized via electron beam (e-beam) evaporation using the glancing angle deposition (GLAD) method. The optimized Au catalytic layer was deposited on the SnO_2 NR surface for the efficient oxidation of VOC molecules. The optimized sensor exhibited significantly higher sensing responses and rapid response times toward BTXF gases compared to other previously reported MOS-based gas sensors. Furthermore, each of the four BTXF gases was selectively detected within 5 min in the mixed gas by integrating the sensor into a miniaturized gas chromatography (mini-GC) system. The sensors exhibited ppb detection limits. These results demonstrate the potential application of the Au-coated SnO_2 sensor as a high-performance indoor air monitoring system.

2. Experimental section

2.1. Fabrication of Au-coated SnO_2 NR sensor devices

Two types of sensor devices were fabricated using Au-SnO_2 NRs. One device evaluated the sensing performance of Au-SnO_2 NRs for each BTXF gas; the device was fabricated on a SiO_2/Si substrate (8.5 × 8.5 mm^2), and its sensing measurement was performed using a tube furnace system. The other was fabricated on an Al_2O_3 substrate (5 × 2.5 mm^2) for the real-time selective detection of each BTXF gas, which was accomplished by integrating it into the mini-GC system. Electrodes in the former device were fabricated by the deposition of Cr (20 nm)/Pt (200 nm) on a thermally oxidized silicon wafer (3000 Å) via a conventional photolithographic process. The latter sensor device comprised interdigitated electrodes (Pt, 100 nm) and a heating circuit (Pt, 600 nm) on the top and bottom sides, respectively. SnO_2 NR arrays were then formed across the interdigitated electrodes via GLAD via e-beam evaporation. Commercial SnO_2 granules (4 N purity, Kojundo Chemical Laboratory Co., Ltd.) were placed in a 7 cc crucible as a SnO_2 source. Vertical SnO_2 NRs were grown on the substrates by tilting the substrate by 80° and rotating at a speed of 12 rpm. The initial pressure of the chamber was maintained at 5.0 × 10^{-6} Torr. The growth rate of NRs was adjusted as 1 Å/s. After deposition, the SnO_2 NR arrays were annealed at 550 °C for 2 h in the ambient air for better adhesion and enhanced crystallinity. Subsequently, the noble metal target, Au, was evaporated and deposited on the SnO_2 NRs via an ultra-high vacuum direct current (DC) sputtering system (SNTEK Co., Ltd.). The chamber pressure was adjusted to 3.4 × 10^{-7} Torr with 34 sccm of Ar flow. The deposition rate was determined to be 0.67 nm/s.

2.2. Characterization of sensing material

SnO_2 NR arrays were characterized via field-emission scanning electron microscopy (FE-SEM, JSM-7610 F-Plus, JEOL) and high-resolution transmission electron microscopy (HR-TEM, JEM-ARM 200 F NEOARM, JEOL). The compositional information of the fabricated samples was obtained through energy-dispersive X-ray spectroscopy (EDS) analysis integrated with FE-SEM and HR-TEM. The crystalline phase and chemical structure of the as-prepared NRs were analyzed using high-resolution X-ray diffraction (HR-XRD, Smartlab, Rigaku) with Cu Kα radiation in the grazing-incidence mode and Raman spectroscopy (LabRam Aramis, Horriba Jovin Yvon) with an excitation laser wavelength of 532 nm. The chemical bonding states and ionic phases of the material surface were evaluated using X-ray photoelectron spectroscopy (XPS, K-alpha, Thermo U. K.) with a monochromated Cu Kα source.

2.3. Evaluation of the sensing performance of Au-coated SnO_2 NRs

The performance of the SnO_2 NR-based gas sensors was tested in a tube furnace system equipped with mass flow controllers (MFCs). The furnace temperature and gas flow rate were automatically controlled using the customized LabView software. All test gases, namely, benzene, toluene, xylene, and formaldehyde, were prepared using standard gases purchased from a company. The concentration of each gas was adjusted using dry synthetic air as the balance gas and by controlling the gas flow rate of the MFCs. Specific concentrations of the target gas and synthetic air as the carrier gas were injected into the chamber at a constant flow rate of 1000 sccm. The electrical resistance of the NRs across the interdigitated electrodes was calculated by measuring the voltage employing a nanovoltmeter (Keithley 2182) using a constant current source (Keithley 6220). The constant current was fixed at 10 nA with a time interval of 1 s. The sensor response was defined as the amplitude of the sensor signal, which was calculated using the following equation:

$$Response \quad (R) = \frac{R_a - R_g}{R_g} = \frac{\Delta R}{R_g} \tag{1}$$

where R_a denotes the maximum resistance of the sensors in an air atmosphere, and R_g is the minimum resistance during exposure to the target gas.

2.4. Investigation of real-time and selective detection of each BTXF gas

The as-prepared sensor device was packaged and positioned in a chamber that was connected to the GC column outlet. The final mini-GC device (19 × 19.5 × 24 cm^3) comprised a sampling loop (1 mL), a packed GC column (Isenlab Inc.), a gas sensing chamber, solenoid valves, and a mini pump. The gas-sensing performance was evaluated by injecting 10 mL of the target gas into the device at a flow rate of 20 sccm, using a mini pump. Gas with the desired concentration was prepared by mixing synthetic air. Of the 10 mL, only 1 mL of gas was filled in the sampling loop for 10 s. This gas mixture was delivered to the packed GC column, followed by separation depending on stationary phase–molecule interactions. During this process, the column was maintained at 25 °C. The detection time of each BTXF gas was adjusted to within 5 min by optimizing the packing material (CarboBlack B), stationary phase (CarboWax 20 M), inner diameter (0.15 cm), and length (30 cm). The packed column conditions were completely different from those used in our previous reports on the detection of other gases, such as isoprene [32], hydrogen [33], and acetone [34]. The operating temperature of the Au-coated SnO_2 NR sensor was adjusted to 150 °C by Joule heating the backside of the substrate using a power supply (600 mWh, UDP-2002, UNiCORN). The sensor signal was obtained from the logarithm of sensor resistance (log(R)). The sensing performance of the mini-GC system was evaluated based on the peak height of the sensor signals, which can expressed as follows:

$$\Delta \text{ Sensor signal} = \Delta \log(R) = \log(R_{air}) - \log(R_{gas}) = \log(R_{air}/R_{gas}) \tag{2}$$

where $\log(R_{air})$ and $\log(R_{gas})$ are the maximum values before and after exposure to the test gas, respectively.

3. Results and discussion

The fabrication process of the Au-coated SnO_2 NR gas sensor device is shown in Fig. 1(a). The overall morphology of the SnO_2 NRs was characterized via SEM (Figs. 1(b) and 1(S), Supporting Information). As shown in Fig. 1(a), before depositing the Au-catalytic layer, the diameter of the SnO_2 NRs was approximately 35 nm, and they had rough surfaces. After the deposition of the catalytic layer, the size of the NRs increased (~50 nm), and they merged with the flattened surfaces. Pillar arrays of SnO_2 with a length of 200 nm are clearly observed in the cross-sectional images. Elemental analysis (EDS) was conducted to determine the distribution of catalytic metal clusters, and Au signals were mostly observed at the top of the NRs (Fig. 1S(b)). Because the elemental analysis in the SEM did not show the Au content at each sidewall of the NRs, we observed individual NRs through HR-TEM (Fig. 1(c)–(d)). According to the dark-phase image of the rod, different contrast materials were formed on the surface of the SnO_2 NRs, presumably Au catalysts. We determined the presence of Au catalysts anchored on the NRs through elemental analysis. As observed from the EDS data in SEM, a

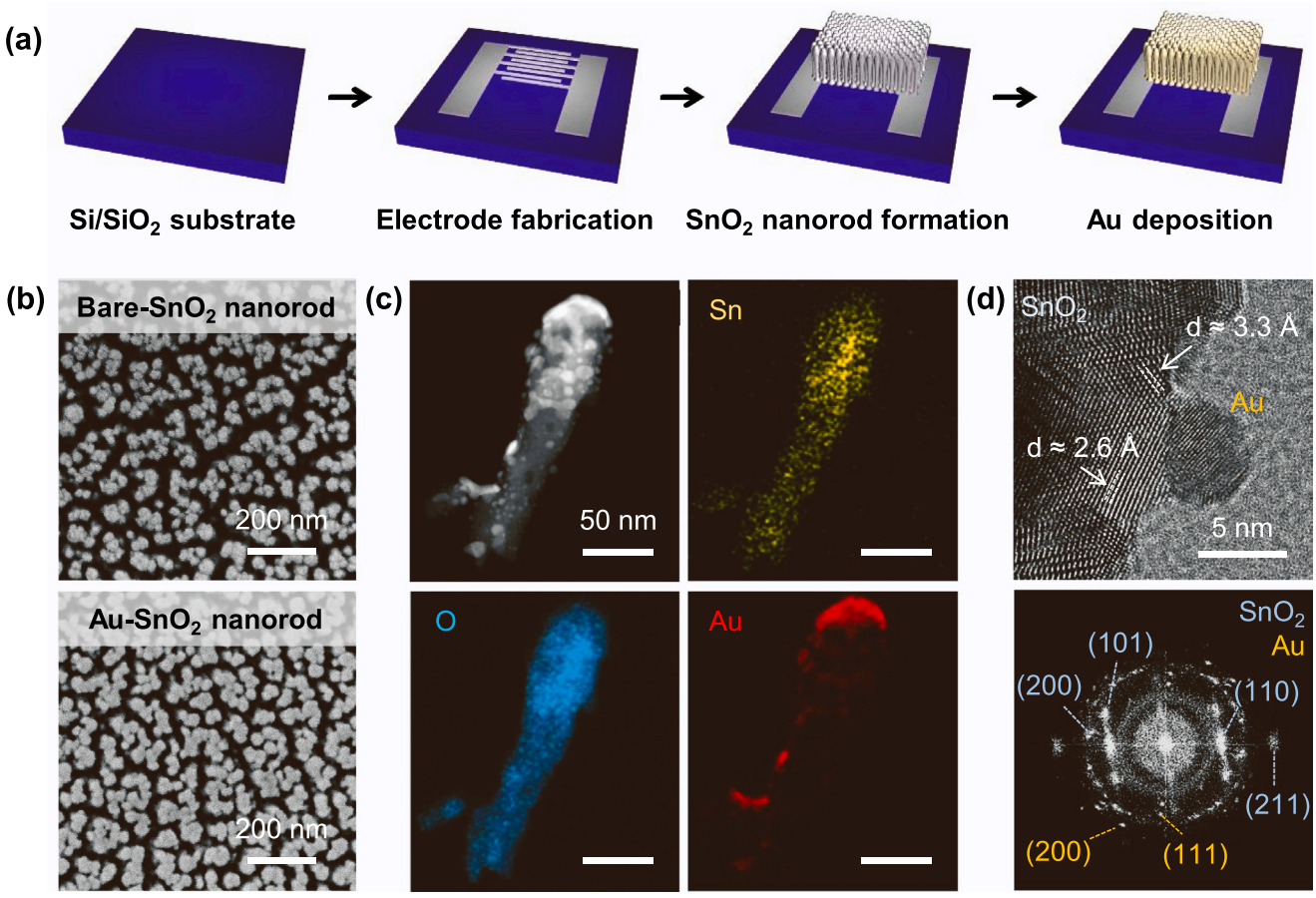

Fig. 1. Visual characterization of Au (5 nm)-coated SnO_2 nanorod arrays. (a) Schematic of the fabrication process of Au-SnO_2 nanorod arrays. (b) Top-view of Au-SnO_2 nanorod arrays before and after Au deposition. (c) Elemental analysis of individual SnO_2 nanorod showing the decoration of the Au catalyst at the sidewall of the nanorod. (d) HR-TEM image of the Au cluster anchored on the sidewall of the nanorod (top). For the SnO_2 lattice structure, d-spacing is clearly shown. Electron diffraction pattern of the Au-SnO_2 showing the crystallographic facet of SnO_2 and Au (bottom).

thick Au layer was formed at the top surface of the NR, and Au-metal clusters (5 nm) were distributed on the side of the NR (Fig. 1(c)). The detailed structure was analyzed at a higher magnification, clearly showing the lattice structure of the NRs and decorated Au particles (top, Fig. 1(d)). The *d*-spacings of 2.6 and 3.3 Å corresponded to the crystalline structure of SnO_2 (101) and (110), respectively. The electron diffraction patterns also confirmed the crystalline structure of Au-SnO_2, and each point could be assigned to specific crystal facets using the inverse fast Fourier transform (FFT) (bottom, Fig. 1(d)).

To further understand the crystallographic properties of the NR arrays, a structural analysis was conducted on the SnO_2 NR arrays at every fabrication step. First, the crystal structure of SnO_2 was analyzed using XRD (Fig. 2(a)). We prepared three types of samples: as-deposited SnO_2 NRs in GLAD e-beam evaporator, heat-treated SnO_2 NRs at 550 °C, and Au-coated SnO_2 NRs. XRD signals were obtained in the grazing-incidence mode, which is a surface-sensitive analysis technique, to evaluate the surface crystalline structure and Au-catalytic layer. As shown in the XRD spectrum (Fig. 2(a)), most of the as-deposited SnO_2 remained in the amorphous phase without showing any crystallinity. The results agreed with the HR-TEM images, which showed that the

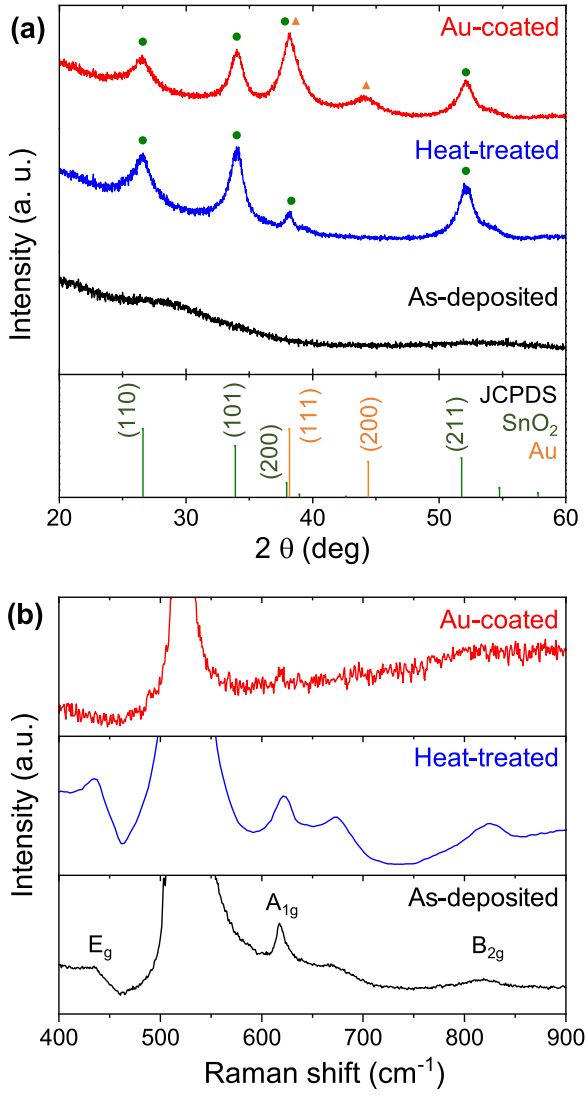

Fig. 2. Structural analysis of SnO_2 nanorods at each fabrication steps. (a) X-ray diffraction (XRD) spectra of as-deposited, heat-treated, and Au (5 nm)-coated SnO_2 nanorod samples. Amorphic SnO_2 are crystallized after heat treatment. Au crystal facets are observed after coating the Au layer. (b) Raman spectra of three samples. Representative Sn-O vibrational modes are observed.

atoms were randomly positioned on the SnO_2 NRs (Fig. S2(a), Supporting Information). After treating the NRs at a high temperature, several diffraction peaks were detected at $2\theta = 26.6°$, 33.9°, 38.1°, and 51.9°, corresponding to the (110), (101), (200), and (211) facets of SnO_2, respectively [35], as shown in Fig. 2(a). These crystal facets were also observed in the electron diffraction patterns shown in Fig. 1(d). In addition, no secondary phases or impurities were observed. These results indicate that the as-deposited SnO_2 NRs were well crystallized after heat treatment. After coating the Au catalytic layer, additional peaks were observed at $2\theta = 38.2°$ and 44.1°, which corresponded to the (111) and (200) facets of the Au lattice, respectively [36] (Fig. 2(a)). A highly crystalline structure of the Au-coated SnO_2 NRs was also observed in the HR-TEM images (Fig. S2(b)). XRD analysis confirmed that heat treatment enhanced the crystallinity of the SnO_2 lattice structure and evenly formed Au-catalytic layers over the entire area of the SnO_2 NRs.

Raman spectroscopy can be used to estimate the crystalline structure of SnO_2 NRs based on the shift and intensity of the intrinsic vibrational modes (Fig. 2b). Similar to XRD analysis, Raman shifts of the as-deposited, heat-treated, and Au-coated SnO_2 NRs were also evaluated. The as-deposited SnO_2 NRs exhibited three vibrational modes at 437, 617, and 822 cm^{-1}. According to previous studies, the rutile structure of the SnO_2 nanoparticle has a symmetric Sn-O vibration mode of A_{1g} (~635 cm^{-1}), asymmetric vibration mode of B_{2g} (~780 cm^{-1}), and fundamental vibration mode of E_g (475 cm^{-1}) [37,38]. The positions of the signals were strongly affected by the size, morphology, and disorder mode. In our study, predicting the peak shift of the unique structure of the SnO_2 NR (length: ~200 nm and diameter: ~50 nm) was challenging; therefore, we assigned the signals at 437, 617, and 822 cm^{-1} to E_g, A_{1g}, and B_{2g}, respectively. These signals were also observed in the heat-treated samples. The results showed that the overall intensity increased, indicating that the crystallinity of SnO_2 was enhanced. The wavenumber of A_{1g} also upshifted after heat treatment (624 cm^{-1}). The enlargement of the NR size can explain this shift owing to the crystallization of the amorphous SnO_2 lattice structure with a specific D-spacing. In the case of the Au-coated SnO_2 NRs, the overall SnO_2 signals disappeared because the Raman-inactive Au layer thoroughly covered the SnO_2 NRs.

The chemical bonding states of the SnO_2 NRs were further analyzed using XPS. We determined the effects of heat treatment on the Sn-O bonding states and Au phase after coating the oxide support through measurements. As shown in Fig. 3(a), Sn 3d (480–500 eV), C 1 s (280–290 eV), and O 1 s (525–535 eV) peaks were observed for all samples [39]. Herein, the small C 1 s signal might be caused by unavoidable carbon sources in the air atmosphere [40]. No significant differences were observed between the spectra of the as-deposited and heat-treated SnO_2 NRs. In the Au-coated sample, Au 4 f (80–90 eV) and Au 4d (320–360 eV) signals appeared considerably stronger than those of Sn 3d and O 1 s owing to the surface intensive analysis performance of XPS [41]. The Au 4 f signal was then deconvoluted to confirm the existence of the Au phase in the sample (Fig. 3b). A previous study demonstrated that Au undergoes a phase transition after being deposited on oxide surfaces by penetrating the oxide lattice through the interface [28]. Most Au preferentially exists in the metallic phase (Au^0), but interfacial Au atoms exist in the Au^+ or Au^{3+} ionic phase, forming Au–O–Sn interactions [42]. In the Au-coated SnO_2 NR sample, a thick Au layer was confirmed at the top surface of the NR, mainly comprising a metallic Au phase (Au^0), but interfacial Au existed in the ionic phase (Au^+ and Au^{3+}). Our deconvolution data confirmed that a small portion of the Au content underwent a phase transition to Au^+ [43].

Oxygen vacancy is a critical factor in determining the gas-sensing performance of MOS-based chemiresistors [7]. This vacancy site is an empty oxygen site in the oxide lattice containing a lone pair of electrons as the electron donor [44]. This site induces the adsorption and ionization of gaseous oxygen molecules, which are active sites for the oxidation of gaseous molecules. In the XPS data, we analyzed the oxygen peak (O 1 s) of the as-deposited, heat-treated, and Au-coated SnO_2 NRs

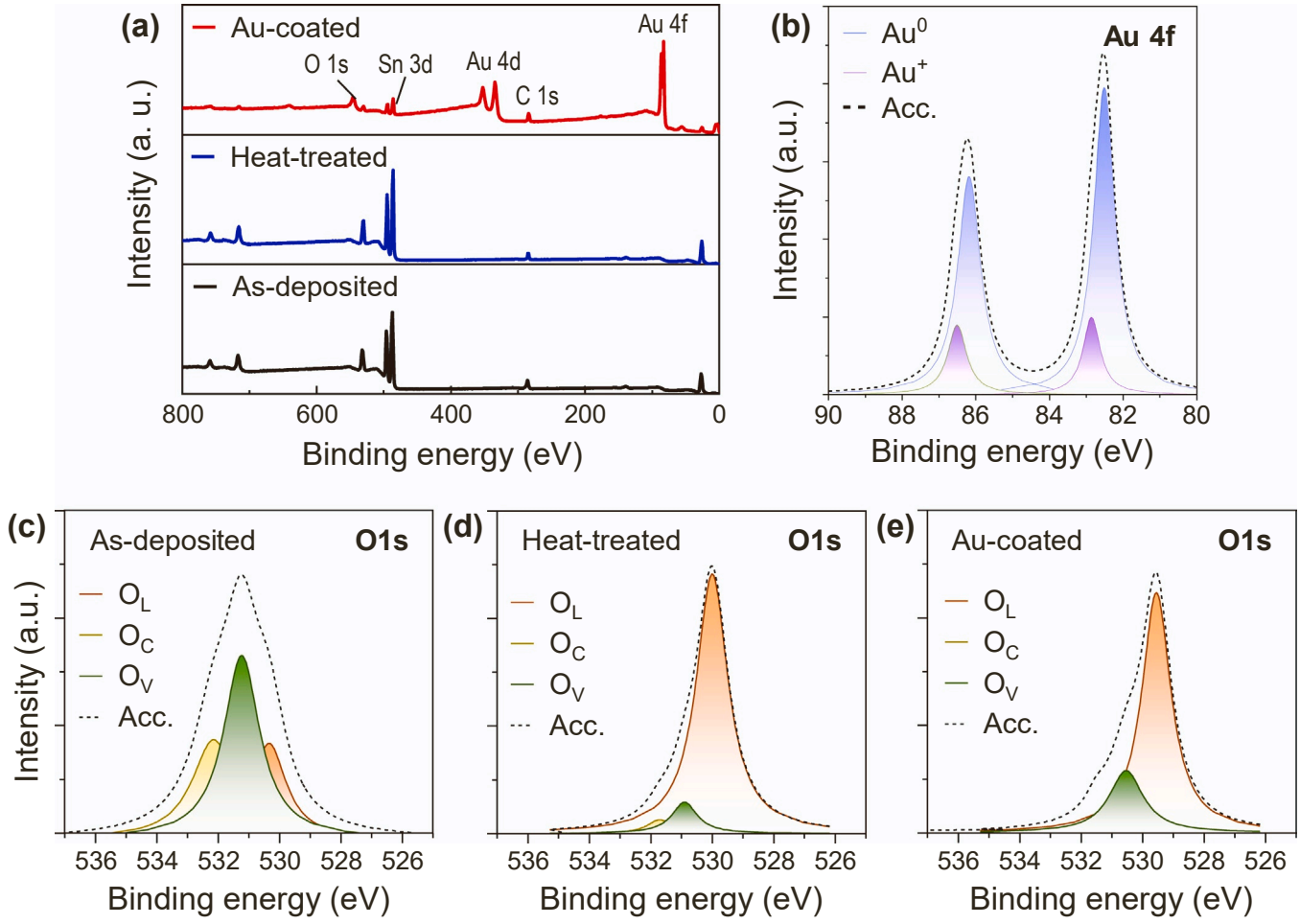

Fig. 3. XPS analysis on various SnO_2 nanorod samples. (a) Measured XPS spectra of as-deposited, heat-treated, and Au (5 nm)-coated SnO_2 nanorod samples. (b) Deconvolution of Au 4 f signal obtained from Au-coated SnO_2 nanorod. O 1 s peak is deconvoluted to determine lattice (O_L, 530 eV), deficient (O_V, 531 eV), and chemisorbed oxygen (O_C, 532 eV) for as-deposited (c), heat-treated (d), and Au-coated SnO_2 nanorods (e).

by deconvoluting the signal into lattice oxygen (O_L, 530 eV), deficient oxygen (O_V, 531 eV), and chemisorbed oxygen (O_C, 532 eV) (Fig. 3(c)–(e)). In the case of the as-deposited SnO_2, O_V was dominant compared to O_L and O_C. According to our previous characterization, the as-deposited sample had a low crystallinity and comprised an amorphous phase. The low proportion of O_L correlated with this property, which indicated a lack of crystallinity in the sample. This stoichiometric imbalance in the lattice was improved through the heat treatment. When the amorphous Sn_xO_y compound was annealed at a high temperature, atmospheric oxygen molecules compensated for the imbalance, improving the crystallinity [45]. In the XPS spectrum of the heat-treated SnO_2, the O_L significantly increased with a decrease in the O_V ratio. This high-quality SnO_2 was further modified by the deposition of the Au catalytic layer. As explained previously, the coated Au layer formed a heterojunction interface, forming the ionic phase of the Au^+ ionic phase. The coated Au cluster withdrew charge density from the oxide via the interface, reducing the oxygen vacancy formation energy at the perimeter sites of the cluster [28]. Ionic Au also entered the Sn-O lattice structure, driving structural distortion [46]. These phenomena caused an increase in the oxygen deficiency at the oxide surface, which correlates with the XPS data. According to the deconvolution results, the oxygen vacancy ratios of the as-deposited, heat-treated, and Au-coated SnO_2 NRs were 46.8%, 8.6%, and 22.0%, respectively.

Coating the oxide structure with noble metals enhances the sensing performance by providing an energetically favorable reaction pathway. However, the catalytic effect is heavily influenced by the loading amount; therefore, we optimized the thickness of the Au layer by observing the sensor response under various conditions of the catalytic layer. We prepared four types of samples: bare and Au 2 nm-, Au 5 nm-, and Au 7 nm-coated SnO_2 NR sensors. The as-prepared SnO_2 NR sensor devices were positioned inside a tube furnace to observe their temperature-dependent sensing responses. Toluene gas (10 ppm) was used as the target gas. Fig. 4(a)–(d) show the sensing resistance curves of each sensor at various operating temperatures (300–500 °C). All sensors showed that the initial resistance of each sensor in air increased with increasing temperature. This trend is attributed to the change in the intrinsic properties of MOSs upon exposure to air. With increasing temperature, the oxygen molecules adsorbed on the surface trap more electrons from the conduction band of the SnO_2 NRs and form different types of oxygen ion species (e.g., O_2^-, O^-, or O^{2-}), according to Eqs. (3)–(6) [47]:

$$O_{2\ (gas)} \rightarrow O_{2\ (ads)} \tag{3}$$

$$O_{2\ (ads)} + e^- \leftrightarrow O_{2\ (ads)}{}^-, T < 150℃ \tag{4}$$

$$O_{2\ (ads)} + e^- \leftrightarrow 2O_{(ads)}{}^-, 150℃ \le T \le 400℃ \tag{5}$$

$$O_{(ads)}{}^- + e^- \leftrightarrow O_{(ads)}{}^{2-}, T > 400℃ \tag{6}$$

The chemisorbed oxygen species on the surface causes changes in the R_a signal. Therefore, R_a increases as the operating temperature increases owing to the formation of a thicker electron depletion layer on the

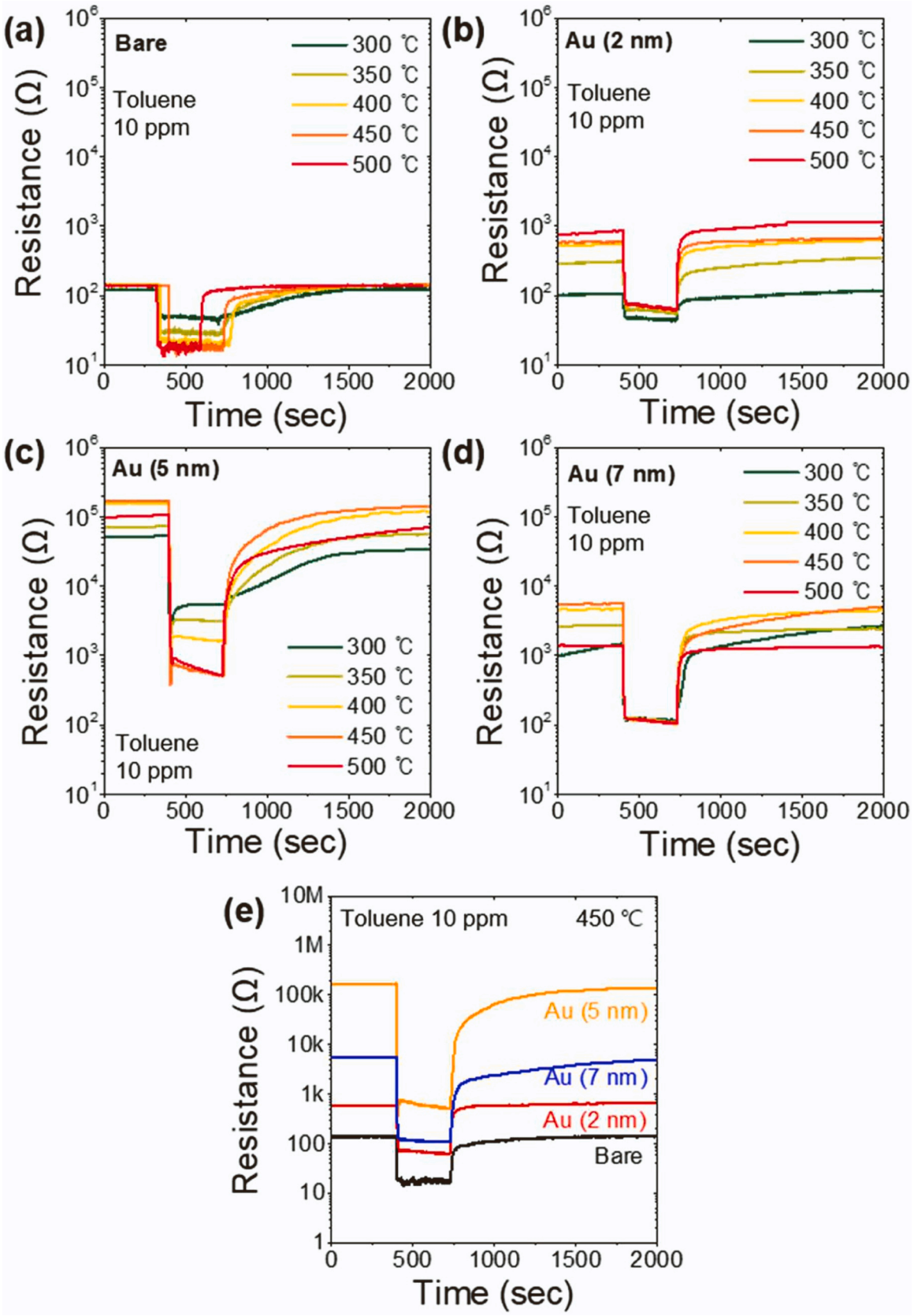

Fig. 4. Sensing resistance of (a) bare, (b) 2-nm-, (c) 5-nm-, and (d) 7-nm-thick-Au-coated SnO_2 nanorod sensors to 10 ppm toluene at various operating temperatures (300–500 ℃). (e) Resistance of all sensors at 450 °C to 10 ppm toluene.

surface of SnO_2 [47]. However, at 500 °C, R_a decreases, as shown in Fig. 4(c)–(d). This can be explained by the fact that, at such a high temperature, the oxygen species fill the oxygen vacancies of SnO_2 after all oxygen molecules are thoroughly adsorbed on the surface [48]. We further compared the resistive behavior of each sensor depending on the Au thickness at the same temperature of 450 °C. As shown in Fig. 4(d), R_a increases with the Au coating thickness. The highest R_a was observed for the SnO_2 NRs coated with 5 nm of Au. This indicates that numerous oxygen ion species were adsorbed on the surface of the 5-nm-thick-Au--coated sensor. The reduction in R_a when the coating thickness was 7 nm suggests that the number of oxygen species adsorption sites are reduced because of the large amount of Au nanoparticles.

Fig. 5(a) shows the sensing response of each sensor prepared with different Au coating thicknesses upon exposure to 10 ppm toluene gas at various operating temperatures (300–500 °C). The highest sensing response ($\Delta R/R_g \approx 327$) was observed for the SnO_2 NRs coated with a 5-nm-thick Au catalyst at an operating temperature of 450 °C. Fig. 5(b) shows the variation in the sensing response over time for the as-prepared SnO_2 NR sensors at 450 °C. As shown in Fig. 5(b), the response of 5-nm-thick-Au-coated sensor was saturated within a few seconds. Based on these results, the thickness of the catalytic layer was optimized at 5 nm. Fig. 5(c) shows the maximum sensing response of the 5-nm-thick-Au-coated SnO_2 NRs (hereafter referred to as Au-SnO_2 NRs) at 10 ppm BTXF in the temperature range of 300–500 °C. Based on the response curves (Fig. S3), the maximum sensing response was determined to be ~662 for formaldehyde at 400 °C, ~328 for toluene at 450 °C, ~170 for xylene at 400 °C, and ~139 for benzene at 500 °C. The response curves in Fig. S3 were obtained from the sensing resistance curves for 10 ppm of each gas at various operating temperatures, as shown in Fig. S4. The sensing response of the Au-SnO_2 NRs was higher for formaldehyde than for the BTX gases tested. In general, the response of n-type MOS gas sensors is higher for highly reactive formaldehyde gases than for the less reactive BTX gases [49]. In addition, the sensing response of the Au-SnO_2 NRs to toluene and xylene was higher than that of benzene. Among the BTX gases, benzene is the most chemically inert, and its sensing response increases with an increase in the number of methyl groups (–CH_3 group) [49]. The methyl groups act as electron-donating groups and increase the electron density on the benzene ring [49]. The redox reaction allowing sensing is more likely to occur in toluene and xylene than the direct dissociation of the benzene ring [49]. Based on the response curve data, the response time was estimated as the time required to reach 90% of the saturated response change. The Au-SnO_2 NRs sensor rapidly detected all the gases within 2.5–3 s for formaldehyde, 1 s for toluene, 1.5 s for benzene, and 1.8 s for xylene (Fig. 5(d)).

To determine the sensitivity and detection limit of the Au-SnO_2 NRs sensor, we measured the sensing performance for various gas concentrations (0.01–10 ppm; Fig. 6). Because we aimed to sensitively detect all these BTXF gases, the experiment was conducted at the temperature at which the highest average response was obtained for the BTXF gases. Because the average sensor response at 450 °C was higher ($\Delta R/R_g \approx 277$) than that at 400 °C ($\Delta R/R_g \approx 241$) (Fig. 5(c)), the measurement was conducted at 450 °C (Fig. 6(a)–(d)). The results confirmed that the

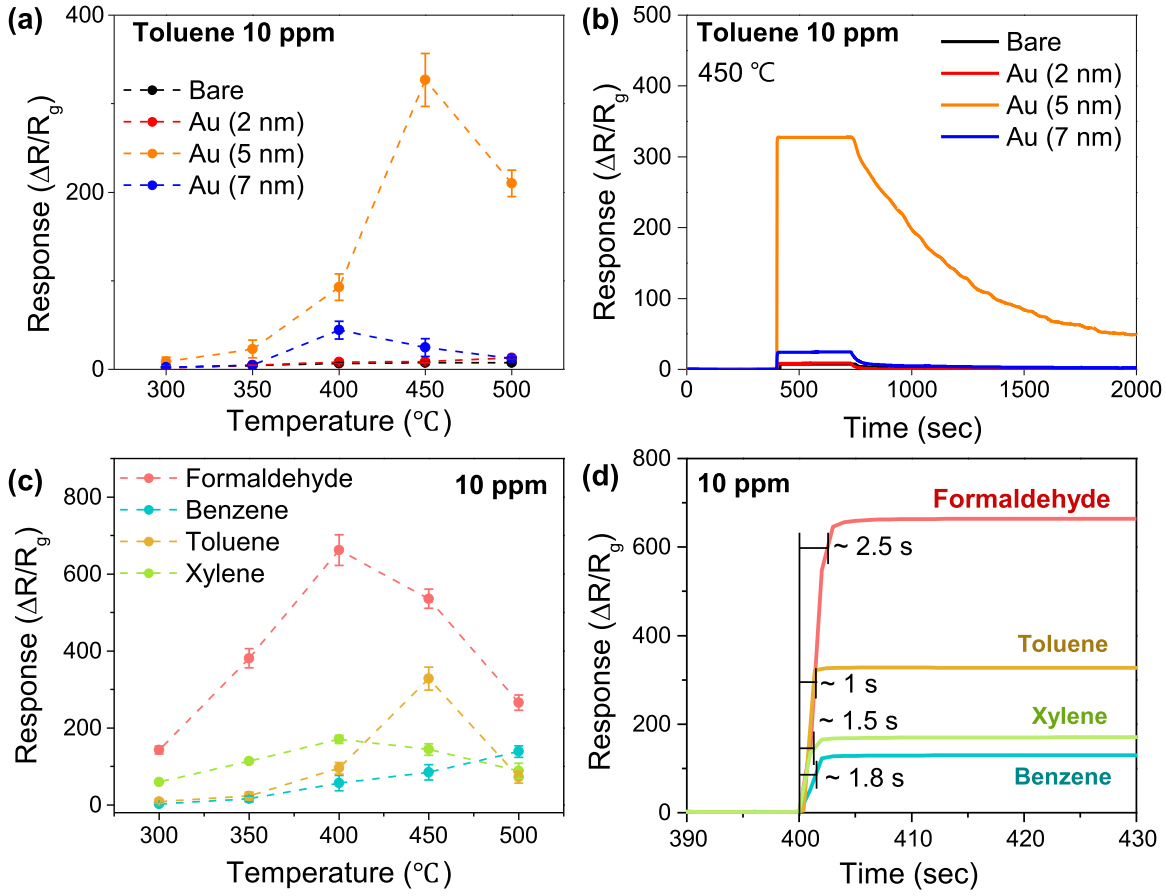

Fig. 5. Catalyst optimization by varying the thickness of the Au layer and sensing performance of the 5-nm-thick-Au-coated SnO_2 nanorod sensor. (a) Maximum response of the bare and Au-coated SnO_2 nanorod sensors for 10 ppm toluene as a function of the operating temperature. Optimal sensing performance is obtained under the 5-nm thickness condition. (b) Response curves of bare, 2-nm-, 5-nm-, and 7-nm-thick-Au-coated SnO_2 nanorod sensors at 450 °C for 10 ppm toluene. (c) Maximum sensing response of 5-nm-thick-Au-coated SnO_2 nanorod sensor for 10 ppm of benzene, toluene, xylene, and formaldehyde at various temperatures (300–500 °C). (d) Response time depending on the gaseous molecule, calculated using the time until the response reaches 90% saturation at the optimal operating temperature.

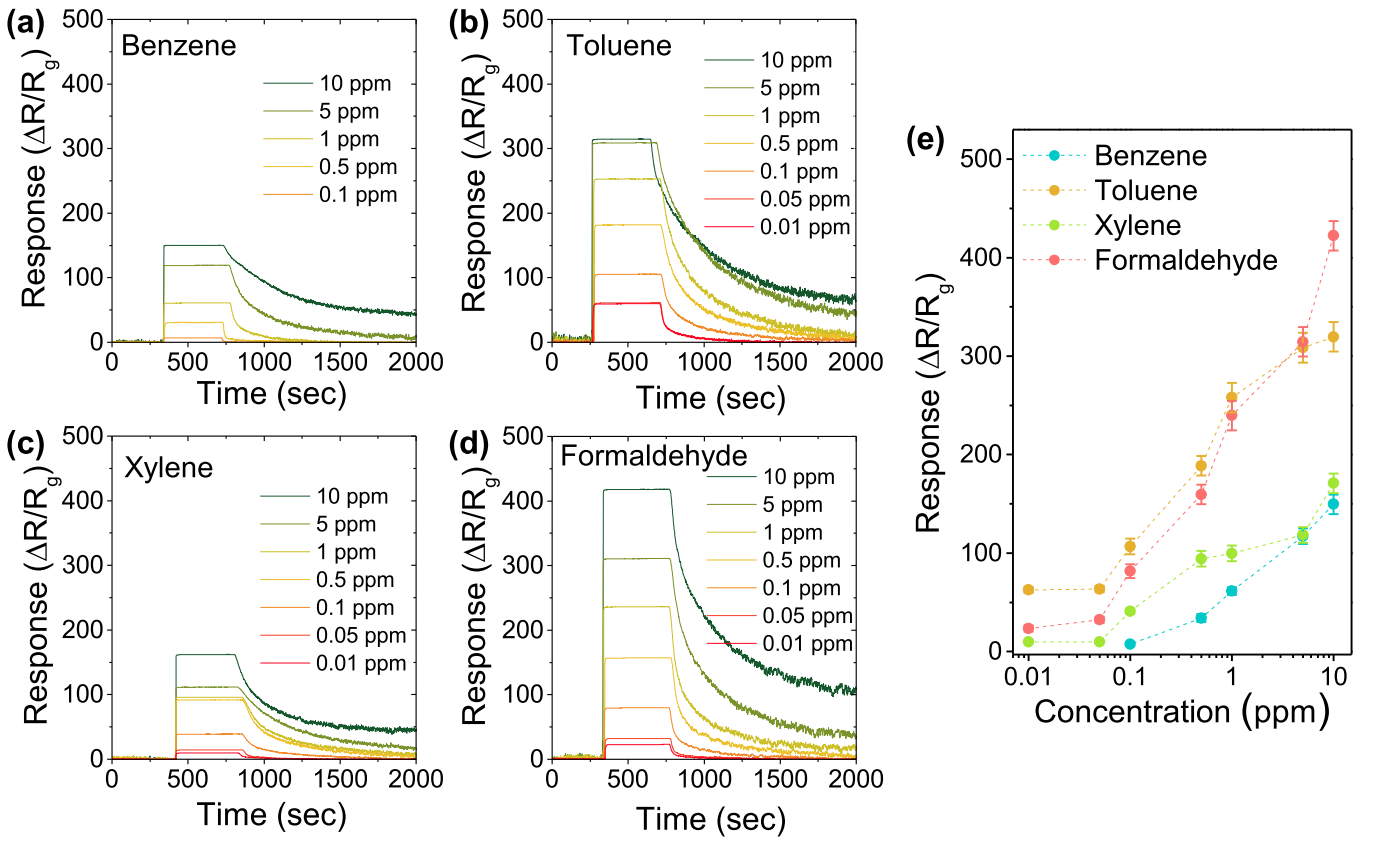

Fig. 6. Variation in the sensing response of the 5-nm-thick-Au-coated SnO_2 nanorod with time for the detection of various gases: (a) benzene, (b) toluene, (c) xylene, and (d) formaldehyde at different concentrations (0.01–10 ppm) at 450 °C. (e) Sensing response to benzene, toluene, xylene, and formaldehyde as a function of gas concentration (0.01–10 ppm) at 450 °C.

response increased linearly with the gas concentration in a log-scale plot (Fig. 6(e)). Herein, xylene, toluene, and formaldehyde were sensitively detected up to 0.01 ppm with sensor responses of ~10, ~63, and ~24, respectively. However, benzene was not detected below the 0.1 ppm concentration. The performance of the sensor is summarized in Fig. 7 and the parameters are listed in Table 1. The optimal operating temperature of the proposed sensor for detecting BTXF gases was relatively high (400–500 °C). However, the sensor responses (~2.7, ~9, ~59, and ~143 for benzene, toluene, xylene, and formaldehyde, respectively (Fig. 4(c)) at the low temperature of 300 °C, which is the optimal operating temperature for other MOS-based sensors (as shown in Table 1), are still high. Therefore, compared with previously reported BTXF gas sensors [50–69], our sensor exhibited superior performance (higher sensitivity, rapid response time, and low detection limit) toward the detection of BTXF gases at concentrations of 0.01–10 ppm.

Real-time and selective detection of each gas component in the gas mixture is essential for minimizing the malfunction of gas sensors induced by the presence of interfering components. Many previous studies have utilized approaches based on structural modification [70–72], chemical coating [73,74], and use of olfactory receptors [75,76] to enhance the selectivity of gas sensors; however, the fabrication of highly selective gas sensors remains technically challenging. Several groups have composed array sensors, identified each response pattern, and used principal component analysis methods. However, the development of algorithms and their utilization are highly limited in real-time analysis upon exposure to gas components [77,78]. Recently, packed-bed columns and filter layers have been used as sensing materials [79–82]. The size exclusion and chemical interaction between the filter phase and gaseous molecules can eliminate undesired components (i.e., humidity and interfering gases) such that only the components of interest can penetrate the filter layer. In a similar approach, we previously reported the integration of a gas sensor into a mini-GC system equipped with a packed column, in which the gas mixtures could be separated depending on the strength of the interaction between the gas molecules and stationary phase. [32]. The column was packed with support materials that were coated with a stationary phase exhibiting weak polarity. A constant flow of dry air, which served as the carrier gas and drove the target gas molecules through the column, was maintained. Therefore, the sensor could separately detect each gas component in sequence from the weakly bonded, nonpolar, and smaller gas molecules (Fig. S5). As the Au-SnO_2 NRs were highly reactive to the four types of VOC gases (BTXF), we applied mini-GC devices to selectively detect each component. The experimental setup is illustrated in Fig. 8(a). For facile integration, the size of the sensor was miniaturized using a 5 × 2.5 mm^2 alumina substrate. The sensor was heated directly by applying a voltage through a Pt heating circuit patterned at the bottom of the substrate. The temperature of the sensor substrate was measured with a contact type thermometer (UT325, Uni-Trend Technology). The optimal working temperature of the sensor, when integrated into the mini-GC device, was determined to be ~150 °C (Fig. 8(b)), which was significantly lower than the temperature measured using the tube furnace system. A lower operating temperature was obtained in a previous study, where a Pd-coated SnO_2 nanorod sensor demonstrated the best sensing performance at 152 °C when integrated into a different mini-GC system employed for hydrogen gas detection [32]. The gas mixture was injected at the inlet of the mini-GC device and the sampling loop contained 1 mL of the target gas. The sampled gas was transferred at a constant flow rate of 20 sccm to a packed GC column maintained at 25 °C to separate the gas components. Finally, the sensor sequentially detected each gas compound from the released compound. A pump located at the end of the gas line is used to control the overall gas flow.

The sensing measurements in the GC-based system differed from

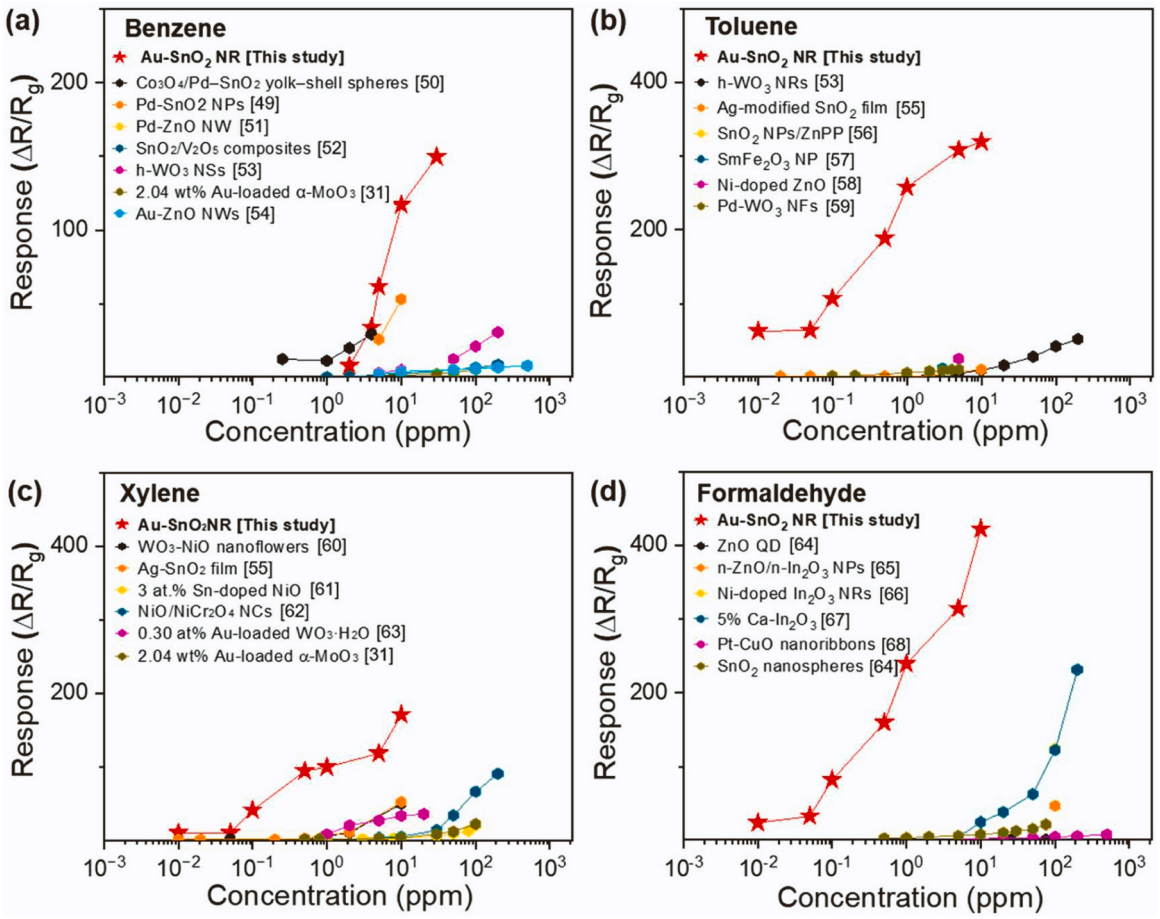

Fig. 7. Gas sensing performance toward the detection of (a) benzene, (b) toluene, (c) xylene, and (d) formaldehyde.

typical sensing measurements (Fig. S6). In the GC-based system, the test gas was injected at a constant flow rate using high-purity synthetic air as the carrier gas. The sensor acted as a detector. In MOS-based materials, the sensing reaction is typically observed through a change in resistance, which occurs due to a change in electron density induced by chemical reactions between the oxygen ion species adsorbed onto the surface of the sensor material and the test gas molecules. Therefore, the sensor signal in the mini-GC system was obtained by calculating the logarithm of the sensor resistance (R), that is, log(R). The sensor in the mini-GC system detected the test gas passing through the column. Consequently, it did not experience a fully saturated response, unlike in the tube-furnace sensing measurements, ensuring its rapid recovery to the initial state even at a lower temperature of 150 °C. The sensor signal was observed as a peak or as a peak along the baseline, as shown in Fig. 8 and Fig. S6. The time corresponding to the peak position was defined as the retention time, which represents the duration between gas injection and detection (Fig. S6(b)). It is influenced by several factors, including the composition of the stationary phase, length and diameter of the column, temperature of the column, and flow rate of the carrier gas. Each gas component possesses a characteristic retention time, which can be employed to identify and quantify the mixture components. As described in the experimental section, the separate detection of each BTXF gas within 5 min was achieved by optimizing the column conditions. Meanwhile, we evaluated the sensing performance of the Au-SnO_2 NRs fabricated on the Al_2O_3 substrate under the same measurement conditions using the tube furnace system. In Fig. S7, we present the resistance variation over time for the Au-SnO_2 NR sensor fabricated on the Al_2O_3 substrate when exposed to 10 ppm of each BTXF gas. Notably, as depicted in Fig. S7, the sensors fabricated on the Al_2O_3 substrate exhibited an almost similar response with the same trend as the sensor fabricated on the SiO_2/Si substrate (Fig. 5(c)), as the temperature increased.

To determine the retention times of BTXF, we conducted a single-gas test using various concentrations (0.001–10 ppm) of each gas (Fig. 8(c)–(f)). The baseline of the sensor fluctuated slightly owing to measurement noise. We verified the assignment of the peak positions by changing the gas concentration. The amplitudes of the signals changed with the gas concentration, but the peak positions were approximately the same, regardless of the concentration. Therefore, the retention times of each gas were determined to be ~47, ~85, and ~248 s for benzene (Fig. 8(c)), toluene (Fig. 8(d)), and xylene (Fig. 8(e)), respectively. In the case of formaldehyde (Fig. 8(f)), three peaks were observed at ~22 (F1), ~82 (F2), and ~110 s (F3), presumably ascribed to the byproducts of highly reactive formaldehyde via photo-oxidation in an ambient air atmosphere [83]. As the concentration decreased, the second peak disappeared and the first and third peaks remained. Therefore, the main formaldehyde sensing peaks were defined as the F1 and F3 peaks. In particular, an unknown peak, indicated by the red circle, was observed for all gases at retention times between 120 and 180 s (Fig. 8(b)–(e)). The peak was identified as a background peak originating from synthetic air used as the balance gas (Fig. S8). As shown in Fig. 8(c)–(f), the BTX gas was detected in the order of benzene, toluene, and xylene according to the characteristics of each gas molecule. The trend of the increase in detection time is related to the molecular weight and dipole moment. Because the stationary phase coated on the packed-column filler had a weak polarity, gases with low molecular weights and weak dipole moments were rapidly released from the column. As shown in Fig. S9, the molecular weight and dipole moment increased in the order of benzene (78.11 g/mol and 0 D), toluene (92.14 g/mol and 0.37 D), and xylene (106.16 g/mol and 0.65 D). However, formaldehyde does

Table 1
Comparison of the sensing performances of various types of metal oxide-based sensors for the detection of benzene, toluene, xylene, and formaldehyde.

Target gas	Sensing material	Operating temperature (℃)	Concentration (ppm)	Response ($\Delta R/R_g$)	Sensitivity[a] (ppm^{-1})	Response time (s)	Detection limit (ppm)	Reference
Benzene	Au-SnO_2 NR	500	10	139	13.9	1.5	< 0.01	This study
	Co_3O_4/Pd–SnO_2 yolk–shell spheres	400	5	99.7	17.6	3	0.25	[50]
	Pd-SnO_2 NPs	400	1	25.5	25.5	-	1	[49]
	Pd-ZnO NW	25	50	2.2	0.044	-	0.1	[51]
	SnO_2/V_2O_5 composites	270	50	5.1	0.045	9	0.5	[52]
	h-WO_3 NSs	320	50	13.0	0.25	36	1	[53]
	2.04 wt% Au-loaded α-MoO_3	250	100	5.3	0.053	-	0.1	[31]
	Au-ZnO NWs	340	10	8.0	0.016	50	1	[54]
Toluene	Au-SnO_2 NR	450	10	328	32.8	1	< 0.01	This study
	h-WO_3 NSs	320	50	27.0	0.56	17	1	[53]
	Ag-modified SnO_2 film	400	10	33.7	3.37	-	0.047	[55]
	SnO_2 and ZnO NPs	300	9	9.0	8	-	0.02	[56]
	$SmFeO_3$ NP	320	5	20.0	4	-	0.01	[57]
	Ni-doped ZnO	350	5	25.7	5.1	-	5	[58]
	Pd-WO_3 NFs	350	1	5.5	0.5	10.9	1	[59]
Xylene	Au-SnO_2 NR	400	10	170	17	1.8	0.1	This study
	WO_3-NiO nanoflowers	300	50	8.1	0.2	51	0.05	[60]
	Ag-SnO_2 film	400	10	54.9	5.49	-	0.042	[55]
	3 at% Sn-doped NiO	225	100	20.2	0.2	298	0.3	[61]
	NiO/$NiCr_2O_4$ NCs	180	10	30.0	0.66	1217	0.05	[62]
	0.3% Au doped $WO_3 \cdot H_2O$	255	5	26.4	5.3	6.3	5	[63]
	2.04 wt% Au-loaded α-MoO_3	250	100	22.1	0.22	1.6	0.5	[31]
Formaldehyde	Au-SnO_2 NR	400	10	662	66.2	2.5	< 0.01	This study
	ZnO QD	25	25	0.4	0.017	30	25	[64]
	n-ZnO/n-In_2O_3 NPs	300	100	46.8	0.47	6	5	[65]
	Ni-doped In_2O_3 nanorods	160	100	124	1.24	1.45	2.5	[66]
	5% Ca-In_2O_3	120	100	116	1.16	1	0.06	[67]
	Pt–CuO nanoribbons	200	500	8.0	0.07	3	5	[68]
	SnO_2 nanospheres	260	10	7.6	0.76	13	0.5	[69]

a sensitivity = response/concentration

not follow this trend because of its considerably lower molecular weight (30.03 g/mol) and significantly higher dipole moment (2.3 D) compared to other gases. The peak height (Δ Sensor signal) of the sensor signal for each gas is shown in Fig. 8(g). The results indicate that the sensing response increased with increasing gas concentration, ranging from 0.001 to 10 ppm. When integrated into the mini-GC device, the Au-SnO_2 NR sensor could detect low levels of 1 ppb for benzene and formaldehyde, 5 ppb for toluene, and 10 ppb for xylene. As the operating temperature decreases, oxygen ion species with a lower number of electrons are adsorbed Eqs. (4)–(6), resulting in a decrease in the change in resistance. Consequently, this leads to a reduced response at 150 °C. However, even at the relatively low temperature of 150 °C, the sensor integrated into the mini-GC system demonstrated exceptional sensing performance, including remarkably low detection limits. This outstanding sensitivity is attributed to the high sensitivity of the Au-SnO_2 NR sensor.

To analyze the sensor performance toward the selective detection of each BTXF gas, three gas mixtures (B-T-X, B-X-F, and B-T-X-F) were prepared. B-T-X represents a gas of 1 ppm of benzene, toluene, and xylene each. B-X-F represents a gas of 1 ppm of benzene, xylene, and formaldehyde each. B-T-X-F represents a gas of 1 ppm of benzene, toluene, xylene, and formaldehyde each. Fig. 8(h) shows the variations in the sensing signal of the Au-SnO_2 NR sensor when exposed to a mixture of gases. To identify the sensing peaks for the mixed gas, the sensing signals for the single gases of benzene, toluene, and xylene with concentrations of 1 and 5 ppm (in Fig. 8(h) are analyzed. In the case of B-T-X and B-X-F, the gas-sensing peaks were clearly observed at their retention times. However, the peaks of toluene (~85 s) and the second peak (F2) of formaldehyde (~82 s) overlapped owing to similar retention times, but formaldehyde could be clearly identified based on the first and third peaks appearing at ~22 (F1) and ~110 s (F3), respectively. When the B-T-X-F gas mixture was tested, four types of gas (1 ppm each) were separately detected. Accordingly, the results demonstrated that our mini-GC device combined with the Au-SnO_2 NR sensor was able to sensitively and selectively detect 1 ppm of each gas in three and four types of BTXF gas mixtures within 5 min. Most studies on sensing performance analysis through the combination of GC and MOS sensors have focused on a single gas, benzene, and toluene [84–87]. Recently, there was one report on the selective detection of a low-concentration BTEX (benzene, toluene, ethylbenzene, and xylene) gas using a GC-MOS sensor [88]. Each BTEX gas (0.3–20 ppb) was individually detected within 11 min using a Au/Pd-coated SnO_2 thin film integrated with a commercial GC system [88]. According to another report, the selective detection of BTEX gas and formaldehyde was possible by combining two types of GC, even using photoionization detectors (PID) rather than MOS-based sensors [89]. Therefore, the separate detection of the four types of BTXF gases within 5 min using a single MOS gas sensor (Au-SnO_2 NRs) and a single GC is the first report.

The detection stability of the mini-GC integrated with the Au-SnO_2 NR sensor was evaluated. The performance of MOS gas sensors mostly deteriorates under high-humidity conditions, because H_2O molecules competitively react with ionized oxygen in the lattice structure [82]. We estimated the sensor performance under 90% humidity by exposing it to 10 ppm benzene gas. A moisture filter was applied to the mini-GC device

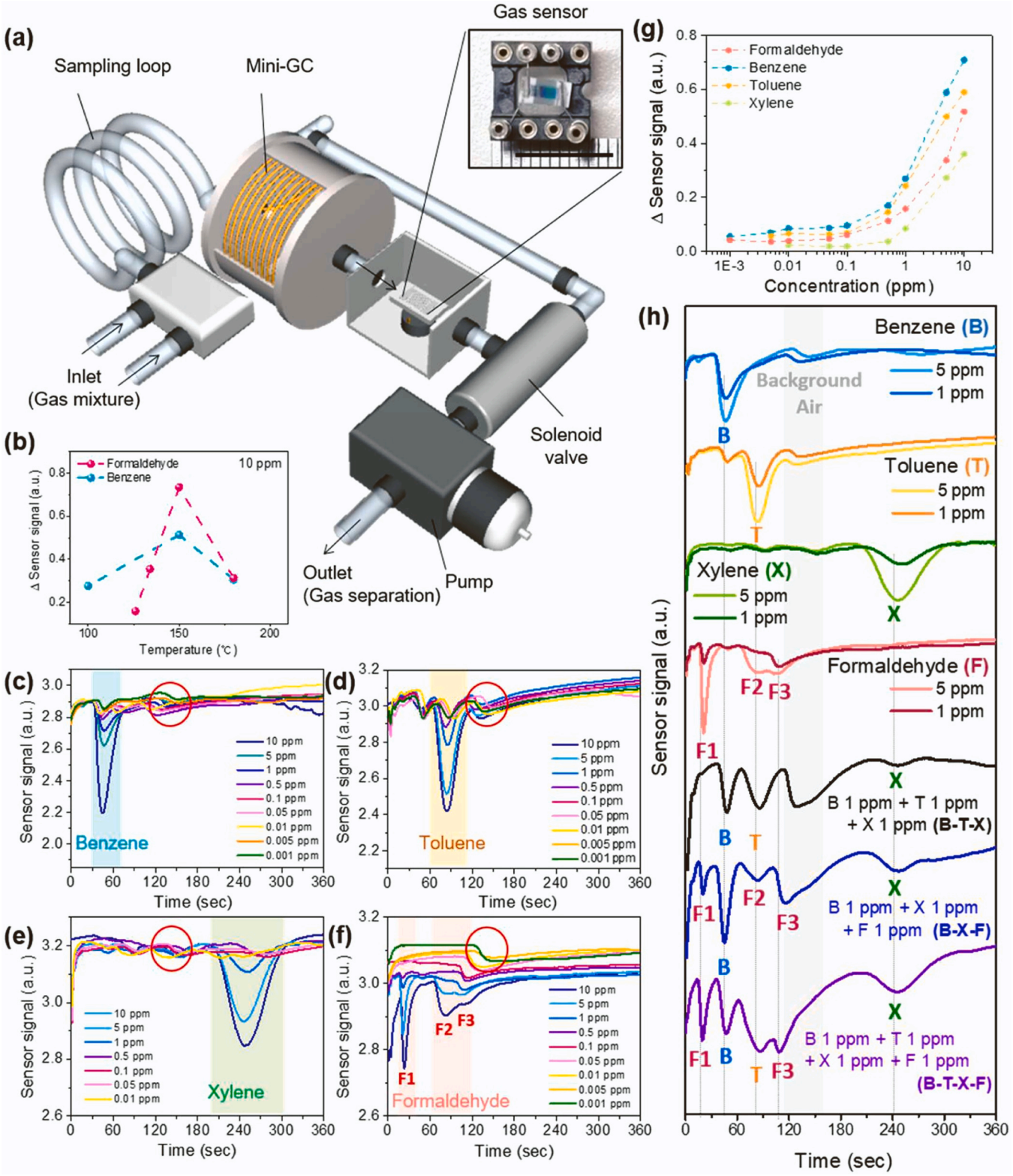

Fig. 8. Sensing performance of 5-nm-thick-Au-coated SnO_2 NR gas sensors integrated into the mini-GC devices. (a) Schematic of the mini-GC device integrated with a packaged gas sensor. Inset shows a picture of the packaged sensor in the device (scale bar: 1 cm). The sensor was Joule-heated to 150 °C using a heating circuit that was patterned on the bottom side of the substrate. The sensor signal was obtained from the logarithm of the sensor resistance (log(R)). (b) Peak height of the sensor signal (Δ Sensor signal) at 10 ppm benzene and formaldehyde as a function of the operating temperature. Sensor signals of the Au-SnO_2 nanorod gas sensors integrated into the mini-GC device at various concentrations (0.001–10 ppm) of (c) benzene, (d) toluene, (e) xylene, and (f) formaldehyde. (g) Peak height of the sensor signal (Δ Sensor signal) at various gas concentrations (0.001–10 ppm) of benzene (B), toluene (T), xylene (X), and formaldehyde (F). (h) Sensor signals for single gases of B, T, X, and F with different concentrations of 1 and 5 ppm, and three types of mixture gases of B-T-X, B-X-F, and B-T-X-F. B-T-X represents a mixed gas of 1 ppm of benzene, toluene, and xylene each. B-X-F represents a mixed gas of 1 ppm of benzene, xylene, and formaldehyde each. B-T-X-F represents a mixed gas of 1 ppm of benzene, toluene, xylene, and formaldehyde each.

to analyze its performance under humid conditions (Fig. 9(a)). The response was measured as 0.45 without the filter and 0.47 with the filter, which was slightly higher under dry conditions. However, the difference was negligible, indicating that the GC column also separated humidity from benzene gas. We also investigated the detection stability by repetitively exposing the sensor to the gas (Fig. 9(b)). Herein, the sensor was exposed to 10 ppm benzene gas for more than 20 times; the results showed that the sensor response did not decrease, even when the gas exposure was repeated several times. Based on these results, we demonstrated the stability of the fabricated sensor system. Fig. 10.

To verify the sensing performance of our mini-GC system incorporating the Au-coated SnO_2 NR sensor, we estimated the formaldehyde and toluene concentrations in real indoor air in an office. The estimated values were crosschecked with those measured using a commercial chromatography apparatus. For precise analysis, air samples were collected in a 2,4-dinitrophenylhydrazine-coated silica gel cartridge and axial-sampling tube filled with Tenax TA to determine the formaldehyde and toluene in air, respectively. As the two types of samplers collected the indoor air, the mini-GC system analyzed it in real time. The formaldehyde and toluene concentrations in the sampled air were analyzed using liquid chromatography (LC, Waters Alliance e2695 HPLC) and gas chromatography (GC, Shimadzu GCMS-QP2010), respectively. The concentrations measured by our mini-GC system were very similar to those measured using LC and GC, with high R-square values of 0.7886 and 0.9786 for formaldehyde and toluene, respectively. These results

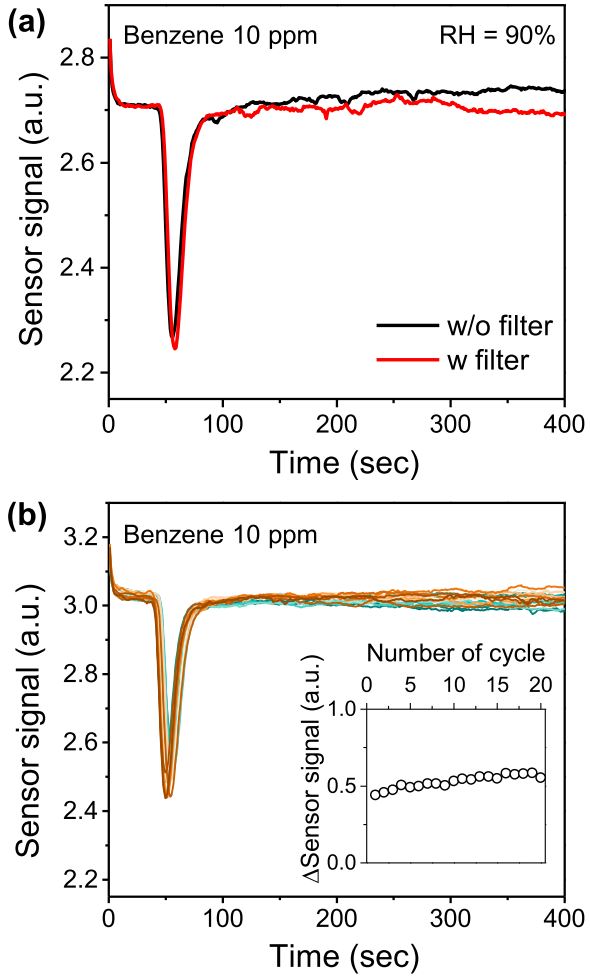

Fig. 9. Sensor stability toward (a) humidity and (b) cycling for sensing 10 ppm benzene. An integrated GC column could reduce the effect of humidity on the sensing performance. Gas sensing performance is maintained even after 20 gas exposure cycles.

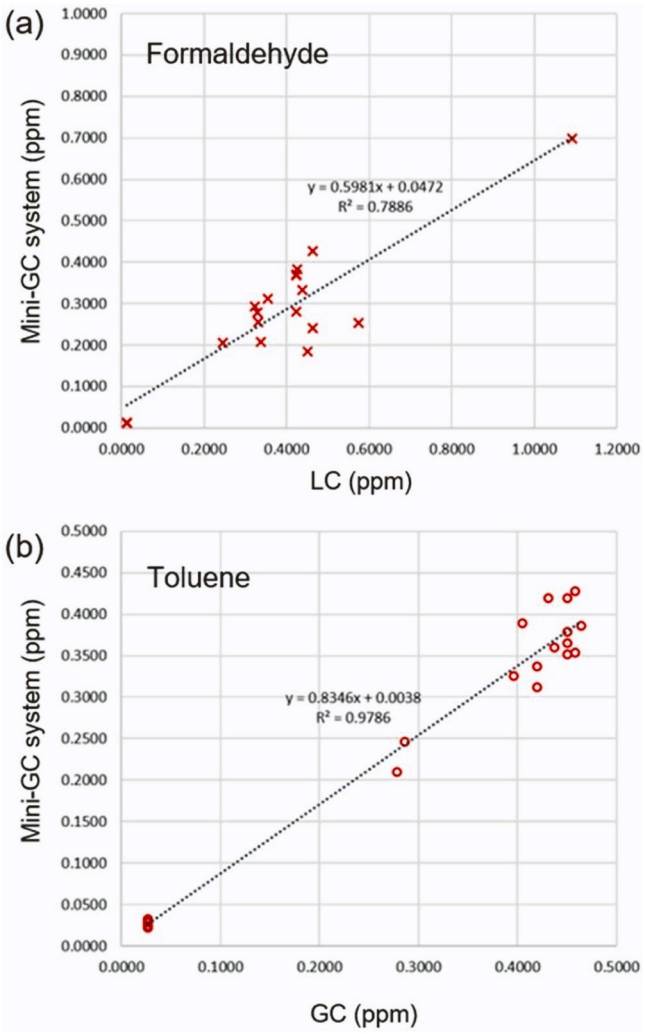

Fig. 10. Reliability test of the mini-GC system equipped with the Au-coated SnO_2 NR gas sensor with the quality analysis of real indoor air from an office. The formaldehyde and toluene in the office indoor air measured by the mini-GC system were compared with the results from commercial precision measurement systems. For the precise analysis of formaldehyde and toluene, liquid chromatography (LC, Waters Alliance e2695 HPLC) and gas chromatography (GC, Shimadzu GCMS-QP2010) were used, respectively.

indicate that the mini-GC system equipped with the Au-coated SnO_2 NR sensor provides a reliable sensing performance.

The outstanding catalytic activity of Au noble metals has been reported and the proposed reaction mechanisms have attracted significant research interest. Catalytic studies have mainly focused on reactions that can occur at the junction interfaces between the Au layer and oxide support [29]. When Au is deposited on the oxide, Au and the oxide form a heterojunction with an interfacial layer [90]. Au shares the lattice position of the oxides at the interface; therefore, several interfacial Au atoms exist in ionic phases, such as Au^{+} and Au^{3+} [91]. This causes lattice distortion with charge imbalance. Because Au has a higher work function (5.35 eV) than most transition metals, it possesses a higher charge density. Charge transfer from the oxide to the Au cluster weakens the bonding strength between the transition metal and oxygen (M-O), which causes an increase in the density of the oxygen vacancies at the perimeter sites of the cluster because the vacancy is a type of electron donor [28]. The gaseous O_2 molecules are then adsorbed to the oxide surface into superoxo (O_2^-) or peroxo (O_2^{2-}) species and finally ionized to O^- and O^{2-} states by obtaining electrons from the vacancy and occupying the lattice site. In this process, an electron depletion layer is formed at

the oxide surface because of the electron transfer from the oxide to oxygen [90]. Ionized oxygen species participate in the oxidation of VOC molecules as reactants. The homogenous Au catalyst without an oxide support mainly oxidizes the target molecule through the Langmuir–Hinshelwood mechanism, which is the reaction between the adsorbed target molecule and oxygen species on the Au surface. However, when Au is anchored on an oxide surface, the reaction pathway changes to the Mars–van Krevelen mechanism [92]. Herein, the O_L at the perimeter of the Au cluster engages in an oxidation reaction with the adsorbed molecules on the Au surface. During the reaction, electrons at the O_L are returned to the oxide, reducing the thickness of electron depletion layer and changing the resistance. Because the reaction occurs at the perimeter site of Au clusters, it is heavily dependent on the size and shape of the cluster. According to a previous study, Au clusters with a size of 4–11 nm significantly enhanced the total oxidation reaction of toluene; however, enhancement of the sensing performance was not observed when the clusters were $>$ 15 nm in size [93]. The densely dispersed nanocluster presumably promoted more O_L atoms to participate in the reaction and provided sufficient time for the molecule to be adsorbed via spill-over effects.

In our study, the enhanced sensing performance of Au-coated SnO_2 NR sensors can be explained by the following factors: According to the visual characterization of the NRs, the top surface of the NRs was covered by a thick and large Au layer, but hemispherical Au nanoclusters (~5 nm) were densely decorated on the sidewall of the rod. In our system, because the mechanically robust NRs were separated from each other with a specific gap, Au clusters could be densely formed at the sidewall of the NR with a narrow size distribution and maintained their conformation, even in a high-temperature environment without any aggregation. The formed Au clusters induced the formation of oxygen vacancies at the perimeter sites of the clusters, promoting the efficient participation of O_L in the oxidation reaction. A spill-over effect was also demonstrated, such that gaseous oxygen molecules were readily adsorbed and ionized at the perimeter sites. Furthermore, the Au cluster is an adsorption site for VOC molecules, providing an effective reaction pathway for the Mars–van Krevelen mechanism. In our XPS deconvolution data, most of the Au is present in the metallic phase. Some studies have reported that metallic Au effectively oxidizes benzene and formaldehyde [94,95]. Studying the detailed sensing mechanisms is challenging at this stage, but the Au coating on SnO_2 NRs significantly contributed to heterogeneous catalytic behavior, resulting in stable sensor operation and significant sensing performance enhancement.

4. Conclusions

This study presents Au-coated SnO_2 NR gas sensors that are highly sensitive to VOC gases, particularly BTXF. Through characterization, we confirmed that the heat treatment of the as-deposited SnO_2 NRs improved the crystallinity of the oxide. Through Au deposition, Au clusters were formed on the sidewalls of the NRs. The clusters enhanced the degree of oxygen vacancies at the perimeter sites, which were the catalytically active sites for the oxidation reaction of VOC molecules. The densely ordered SnO_2 NR arrays provided ideal conditions for heterogeneous catalysts owing to their mechanical robustness, high surface area, and easy reducibility. After optimizing the Au-coated SnO_2 NR gas sensors, the sensor exhibited excellent sensing performance, including a high response and rapid response time of $<$ 2.5 s, for the detection of 10 ppm of each gas. The maximum sensing responses were ~662, ~328, ~170, and ~139 for formaldehyde (400 °C), toluene (450 °C), xylene (400 °C), and benzene (500 °C), respectively, which are significantly higher than those of previously reported MOS-based sensors. The Au-coated SnO_2 NR sensor was integrated into a mini-GC device to investigate the selective detection of each gaseous compound in a BTXF gas mixture. After optimizing the column, we successfully separated the four types of gases into a mixed gas within 5 min. Furthermore, the sensor could sensitively detect up to ppb-level concentrations of each gas. The stability of the sensing system was verified via humidity and repeated tests. Our results demonstrate that a mini-GC device integrated with a sensitive Au-coated SnO_2 NR sensor can be utilized as an indoor air quality monitoring system.

CRediT authorship contribution statement

Jihyun Lee: Conceptualization, Investigation, Visualization, **Hyegi Min**: Conceptualization, Investigation, Visualization, Writing-Original draft preparation. **Yong-Sahm Choe**: Validation, Visualization, **Yun Gyu Lee:** Validation, Visualization, **Kichul Kim:** Conceptualization, Validation, Visualization, **Hyun-Sook Lee:** Conceptualization, Validation, Writing-Original draft preparation, Writing-Review & Editing preparation., **Wooyoung Lee:** Supervision.

Declaration of Competing Interest

The authors declare that they have no known competing financial interests or personal relationships that could have appeared to influence the work reported in this paper.

Data Availability

Data will be made available on request.

Acknowledgement

This research was supported by the Technology Innovation Program (‘20013621’, Center for Super Critical Material Industrial Technology) funded by the Ministry of Trade, Industry & Energy (MOTIE, Korea) and the Basic Science Research Program (NRF-2019R1A6A1A11055660, Key Research Institutes in Universities) and the Nano-Material Technology Development Program (NRF-2022M3H4A3053304, National Core Materials Research Center (Platform type)) through the National Research Foundation of Korea (NRF) funded by the Ministry of Science and ICT(MSIT). This research was also funded by an internal grant (code: 20210449) of the Korea Institute of Civil Engineering and Building Technology (KICT). H.-S. Lee acknowledges the support from the Basic Research in Science and Engineering Program of the NRF (2021R1A2C1013690). H. Min thanks the Korea Initiative for fostering the University of Research and Innovation Program of the NRF (2020M3H1A1077207).

Appendix A. Supporting information

Supplementary data associated with this article can be found in the online version at doi:10.1016/j.snb.2023.134359.

References

[1] K. Harada, A. Hasegawa, C.N. Wei, K. Minamoto, Y. Noguchi, K. Hara, et al., A review of indoor air pollution and health problems from the viewpoint of environmental hygiene: focusing on the studies of indoor air environment in japan compared to those of foreign countries, J. Health Sci. 56 (2010) 488–501.
[2] H.X. Lu, S. Wen, Y.L. Feng, X.N. Wang, X.H. Bi, G.Y. Sheng, et al., Indoor and outdoor carbonyl compounds and BTEX in the hospitals of Guangzhou, China, Sci. Total Environ. 368 (2006) 574–584.
[3] W. Filipiak, A. Filipiak, A. Sponring, T. Schmid, B. Zelger, C. Ager, et al., Comparative analyses of volatile organic compounds (VOCs) from patients, tumors and transformed cell lines for the validation of lung cancer-derived breath markers, J. Breath. Res. 8 (2014), 027111.
[4] H. Guo, S.C. Lee, L.Y. Chan, W.M. Li, Risk assessment of exposure to volatile organic compounds in different indoor environments, Environ. Res. 94 (2004) 57–66.
[5] J. Saini, M. Dutta, G. Marques, A comprehensive review on indoor air quality monitoring systems for enhanced public health, Sustain. Environ. Res. 30 (2020) 1–12.
[6] T. Salthammer, Very volatile organic compounds: an understudied class of indoor air pollutants, Indoor air 26 (2016) 25–38.
[7] H. Ji, W. Zeng, Y. Li, Gas sensing mechanisms of metal oxide semiconductors: a focus review, Nanoscale 11 (2019) 22664–22684.

[8] J.F. Weaver, Surface chemistry of late transition metal oxides, Chem. Rev. 113 (2013) 4164–4215.
[9] A. Dey, Semiconductor metal oxide gas sensors: a review, Mater. Sci. Eng.: B 229 (2018) 206–217.
[10] H. Long, A. Harley-Trochimczyk, S. Cheng, H. Hu, W.S. Chi, A. Rao, et al., Nanowire-assembled hierarchical $ZnCo_2O_4$ microstructure integrated with a low-power microheater for highly sensitive formaldehyde detection, ACS Appl. Mater. Interfaces 8 (2016) 31764–31771.
[11] Z. Tao, Y. Li, B. Zhang, G. Sun, M. Xiao, H. Bala, et al., Synthesis of urchin-like In_2O_3 hollow spheres for selective and quantitative detection of formaldehyde, Sens. Actuators B: Chem. 298 (2019), 126889.
[12] S. Tian, X. Ding, D. Zeng, S. Zhang, C. Xie, Pore-size-dependent sensing property of hierarchical SnO_2 mesoporous microfibers as formaldehyde sensors, Sensors and Actuators B: Chemical 186 (2013) 640–647.
[13] W. Zhang, X. Cheng, X. Zhang, Y. Xu, S. Gao, H. Zhao, et al., High selectivity to ppb-level HCHO sensor based on mesoporous tubular SnO_2 at low temperature, Sens. Actuators B: Chem. 247 (2017) 664–672.
[14] X. Gao, F. Li, R. Wang, T. Zhang, A formaldehyde sensor: Significant role of pn heterojunction in gas-sensitive core-shell nanofibers, Sens. Actuators B: Chem. 258 (2018) 1230–1241.
[15] N. Li, Y. Fan, Y. Shi, Q. Xiang, X. Wang, J. Xu, A low temperature formaldehyde gas sensor based on hierarchical SnO/SnO_2 nano-flowers assembled from ultrathin nanosheets: synthesis, sensing performance and mechanism, Sens. Actuators B: Chem. 294 (2019) 106–115.
[16] J. Sun, L. Sun, S. Bai, H. Fu, J. Guo, Y. Feng, et al., Pyrolyzing Co/Zn bimetallic organic framework to form pn heterojunction of Co_3O_4/ZnO for detection of formaldehyde, Sens. Actuators B: Chem. 285 (2019) 291–301.
[17] L.-Y. Zhu, K. Yuan, J.-G. Yang, H.-P. Ma, T. Wang, X.-M. Ji, et al., Fabrication of heterostructured p-CuO/n-SnO_2 core-shell nanowires for enhanced sensitive and selective formaldehyde detection, Sens. Actuators B: Chem. 290 (2019) 233–241.
[18] R.L. Fomekong, H.T. Kamta, J.N. Lambi, D. Lahem, P. Eloy, M. Debliquy, et al., A sub-ppm level formaldehyde gas sensor based on Zn-doped NiO prepared by a co-precipitation route, J. Alloy. Compd. 731 (2018) 1188–1196.
[19] J. Hu, T. Wang, Y. Wang, D. Huang, G. He, Y. Han, et al., Enhanced formaldehyde detection based on Ni doping of SnO_2 nanoparticles by one-step synthesis, Sens. Actuators B: Chem. 263 (2018) 120–128.
[20] Y.J. Kwon, H.W. Kim, W.C. Ko, H. Choi, Y.-H. Ko, Y.K. Jeong, Laser-engineered oxygen vacancies for improving the NO_2 sensing performance of SnO_2 nanowires, J. Mater. Chem. A 7 (2019) 27205–27211.
[21] J.H. Bang, Y.J. Kwon, J.-H. Lee, A. Mirzaei, H.Y. Lee, H. Choi, S.S. Kim, Y.K. Jeong, H.W. Kim, Proton-beam engineered surface-point defects for highly sensitive and reliable NO_2 sensing under humid environments, J. Hazard. Mater. 416 (2021), 125841.
[22] Z. Han, Y. Qi, Z. Yang, H. Han, Y. Jiang, W. Du, et al., Recent advances and perspectives on constructing metal oxide semiconductor gas sensing materials for efficient formaldehyde detection, J. Mater. Chem. C. 8 (2020) 13169–13188.
[23] S.M. Majhi, A. Mirzaei, H.W. Kim, S.S. Kim, T.W. Kim, Recent advances in energy-saving chemiresistive gas sensors: a review, Nano Energy 79 (2021), 105369.
[24] L. Liotta, Catalytic oxidation of volatile organic compounds on supported noble metals, Appl. Catal. B: Environ. 100 (2010) 403–412.
[25] M.M. Montemore, M.A. van Spronsen, R.J. Madix, C.M. Friend, O_2 activation by metal surfaces: implications for bonding and reactivity on heterogeneous catalysts, Chem. Rev. 118 (2017) 2816–2862.
[26] P. Gélin, M. Primet, Complete oxidation of methane at low temperature over noble metal based catalysts: a review, Appl. Catal. B: Environ. 39 (2002) 1–37.
[27] J. Li, H. Liu, Y. Deng, G. Liu, Y. Chen, J. Yang, Emerging nanostructured materials for the catalytic removal of volatile organic compounds, Nanotechnol. Rev. 5 (2016) 147–181.
[28] A. Ruiz Puigdollers, P. Schlexer, S. Tosoni, G. Pacchioni, Increasing oxide reducibility: the role of metal/oxide interfaces in the formation of oxygen vacancies, Acs Catal. 7 (2017) 6493–6513.
[29] S. Scirè, L.F. Liotta, Supported gold catalysts for the total oxidation of volatile organic compounds, Appl. Catal. B: Environ. 125 (2012) 222–246.
[30] Y. Li, H. Jin, G. Sun, B. Zhang, N. Luo, L. Lin, et al., Synthesis of novel porous ZnO octahedrons and their improved UV-light activated formaldehyde-sensing performance by Au decoration, Phys. E: Low. -Dimens. Syst. Nanostruct. 106 (2019) 40–44.
[31] L. Sui, X. Zhang, X. Cheng, P. Wang, Y. Xu, S. Gao, et al., Au-loaded hierarchical MoO_3 hollow spheres with enhanced gas-sensing performance for the detection of BTX (benzene, toluene, and xylene) and the sensing mechanism, ACS Appl. Mater. Interfaces 9 (2017) 1661–1670.
[32] H. Jung, H. Min, J. Hwang, J. Kim, Y.-S. Choe, H.-S. Lee, W. Lee, Selective detection of sub-1-ppb level isoprene using Pd-coated In_2O_3 thin film integrated in portable gas chromatography, Appl. Surf. Sci. 586 (2022), 152827.
[33] H. Jung, J. Hwang, Y.-S. Choe, H.-S. Lee, W. Lee, Highly sensitive and selective detection of hydrogen using pd-coated sno2 nanorod arrays for breath-analyzer applications, Sensors 22 (2022) 2056.
[34] H. Jung, W. Cho, R. Yoo, H.-S. Lee, Y.-S. Choe, J.Y. Jeon, W. Lee, Highly selective real-time detection of breath acetone by using ZnO quantum dots with a miniaturized gas chromatographic column, Sens. Actuators B: Chem. 274 (2018) 527–532.
[35] G.J. McCarthy, J.M. Welton, X-ray diffraction data for SnO_2, Illus. N. Powder data Eval. Methods, Powder Diffr. 4 (1989) 156–159.
[36] H.F. McMurdie, M.C. Morris, E.H. Evans, B. Paretzkin, W. Wong-Ng, L. Ettlinger, et al., Standard X-ray diffraction powder patterns from the JCPDS research associateship, Powder Diffr. 1 (1986) 64–77.
[37] S. Sun, G. Meng, G. Zhang, T. Gao, B. Geng, L. Zhang, et al., Raman scattering study of rutile SnO_2 nanobelts synthesized by thermal evaporation of Sn powders, Chem. Phys. Lett. 376 (2003) 103–107.
[38] A. Dieguez, A. Romano-Rodrıguez, A. Vila, J. Morante, The complete Raman spectrum of nanometric SnO_2 particles, J. Appl. Phys. 90 (2001) 1550–1557.
[39] M.A. Stranick, A. Moskwa, SnO_2 by XPS, Surf. Sci. Spectra 2 (1993) 50–54.
[40] N. Comini, T. Huthwelker, J.T. Diulus, J. Osterwalder, Z. Novotny, Factors influencing surface carbon contamination in ambient-pressure x-ray photoelectron spectroscopy experiments, J. Vac. Sci. Technol. A: Vac., Surf., Films 39 (2021), 043203.
[41] S. Peters, S. Peredkov, M. Neeb, W. Eberhardt, M. Al-Hada, Size-dependent XPS spectra of small supported Au-clusters, Surf. Sci. 608 (2013) 129–134.
[42] H.Y. Kim, H.M. Lee, G. Henkelman, CO oxidation mechanism on CeO_2-supported Au nanoparticles, J. Am. Chem. Soc. 134 (2012) 1560–1570.
[43] R.R. Krishnan, V. Kavitha, M.S. Kumar, K. Gopchandran, V.M. Pillai, Properties of Au incorporated In_2O_3 films, Mater. Sci. Semicond. Process. 93 (2019) 134–147.
[44] G. Pacchioni, Oxygen vacancy: the invisible agent on oxide surfaces, ChemPhysChem 4 (2003) 1041–1047.
[45] C. Drouilly, J.-M. Krafft, F. Averseng, S. Casale, D. Bazer-Bachi, C. Chizallet, et al., ZnO oxygen vacancies formation and filling followed by in situ photoluminescence and in situ EPR, J. Phys. Chem. C. 116 (2012) 21297–21307.
[46] H.-Y. Lai, C.-H. Chen, Highly sensitive room-temperature CO gas sensors: Pt and Pd nanoparticle-decorated In_2O_3 flower-like nanobundles, J. Mater. Chem. 22 (2012) 13204–13208.
[47] N. Barsan, U. Weimar, Conduction model of metal oxide gas sensors, J. Electroceram. 7 (2001) 143–167.
[48] N. Yamazoe, J. Fuchigami, M. Kishikawa, et al., Interactions of tin oxide surface with O_2, H_2O and H_2, Surf. Sci. 86 (1979) 335–344.
[49] A. Mirzaei, J.H. Kim, H.W. Kim, S.S. Kim, Resistive-based gas sensors for detection of benzene, toluene and xylene (BTX) gases: a review, J. Mater. Chem. C. 6 (2018) 4342–4370.
[50] S.-Y. Jeong, J.-W. Yoon, T.-H. Kim, H.-M. Jeong, C.-S. Lee, Y.C. Kang, et al., Ultra-selective detection of sub-ppm-level benzene using Pd–SnO_2 yolk–shell micro-reactors with a catalytic Co_3O_4 overlayer for monitoring air quality, J. Mater. Chem. A 5 (2017) 1446–1454.
[51] J.-H. Kim, J.-H. Lee, Y. Park, J.-Y. Kim, A. Mirzaei, H.W. Kim, et al., Toluene-and benzene-selective gas sensors based on Pt-and Pd-functionalized ZnO nanowires in self-heating mode, Sens. Actuators B: Chem. 294 (2019) 78–88.
[52] F. Zhang, X. Wang, J. Dong, N. Qin, J. Xu, Selective BTEX sensor based on a SnO_2/V_2O_5 composite, Sens. Actuators B: Chem. 186 (2013) 126–131.
[53] D. Zhang, Y. Fan, G. Li, Z. Ma, X. Wang, Z. Cheng, et al., Highly sensitive BTEX sensors based on hexagonal WO_3 nanosheets, Sens. Actuators B: Chem. 293 (2019) 23–30.
[54] L. Wang, S. Wang, M. Xu, X. Hu, H. Zhang, Y. Wang, et al., A Au-functionalized ZnO nanowire gas sensor for detection of benzene and toluene, Phys. Chem. Chem. Phys. 15 (2013) 17179–17186.
[55] J. Wang, S. Gao, C. Zhang, Q. Zhang, Z. Li, S. Zhang, A high throughput platform screening of ppb-level sensitive materials for hazardous gases, Sens. Actuators B: Chem. 276 (2018) 189–203.
[56] B. Cho, K. Lee, S. Pyo, J. Kim, Fabrication and characterization of VOC sensor array based on SnO_2 and ZnO nanoparticles functionalized by metalloporphyrins, Micro Nano Syst. Lett. 6 (2018) 1–6.
[57] M. Mori, Y. Itagaki, J. Iseda, Y. Sadaoka, T. Ueda, H. Mitsuhashi, et al., Influence of VOC structures on sensing property of $SmFeO_3$ semiconductive gas sensor, Sens. Actuators B: Chem. 202 (2014) 873–877.
[58] H.-S. Woo, C.-H. Kwak, J.-H. Chung, J.-H. Lee, Highly selective and sensitive xylene sensors using Ni-doped branched ZnO nanowire networks, Sens. Actuators B: Chem. 216 (2015) 358–366.
[59] N.-H. Kim, S.-J. Choi, D.-J. Yang, J. Bae, J. Park, I.-D. Kim, Highly sensitive and selective hydrogen sulfide and toluene sensors using Pd functionalized WO_3 nanofibers for potential diagnosis of halitosis and lung cancer, Sens. Actuators B: Chem. 193 (2014) 574–581.
[60] H. Gao, Q. Yu, K. Chen, P. Sun, F. Liu, X. Yan, et al., Ultrasensitive gas sensor based on hollow tungsten trioxide-nickel oxide (WO_3-NiO) nanoflowers for fast and selective xylene detection, J. Colloid Interface Sci. 535 (2019) 458–468.
[61] H. Gao, D. Wei, P. Lin, C. Liu, P. Sun, K. Shimanoe, et al., The design of excellent xylene gas sensor using Sn-doped NiO hierarchical nanostructure, Sens. Actuators B: Chem. 253 (2017) 1152–1162.
[62] H. Gao, J. Guo, Y. Li, C. Xie, X. Li, L. Liu, et al., Highly selective and sensitive xylene gas sensor fabricated from NiO/$NiCr_2O_4$ pp nanoparticles, Sens. Actuators B: Chem. 284 (2019) 305–315.
[63] F. Li, S. Guo, J. Shen, L. Shen, D. Sun, B. Wang, et al., Xylene gas sensor based on Au-loaded WO_3·H_2O nanocubes with enhanced sensing performance, Sens. Actuators B: Chem. 238 (2017) 364–373.
[64] Q. Huang, D. Zeng, H. Li, C. Xie, Room temperature formaldehyde sensors with enhanced performance, fast response and recovery based on zinc oxide quantum dots/graphene nanocomposites, Nanoscale 4 (2012) 5651–5658.
[65] L. Ma, H. Fan, H. Tian, J. Fang, X. Qian, The n-ZnO/n-In_2O_3 heterojunction formed by a surface-modification and their potential barrier-control in methanal gas sensing, Sens. Actuators B: Chem. 222 (2016) 508–516.
[66] X. Zhang, D. Song, Q. Liu, R. Chen, J. Hou, J. Liu, et al., Designed synthesis of Ag-functionalized Ni-doped In_2O_3 nanorods with enhanced formaldehyde gas sensing properties, J. Mater. Chem. C. 7 (2019) 7219–7229.
[67] Q. Liang, X. Zou, H. Chen, M. Fan, G.-D. Li, High-performance formaldehyde sensing realized by alkaline-earth metals doped In_2O_3 nanotubes with optimized surface properties, Sens. Actuators B: Chem. 304 (2020), 127241.

[68] X. Gou, G. Wang, J. Yang, J. Park, D. Wexler, Chemical synthesis, characterisation and gas sensing performance of copper oxide nanoribbons, J. Mater. Chem. 18 (2008) 965–969.
[69] Z. Li, Q. Zhao, W. Fan, J. Zhan, Porous SnO_2 nanospheres as sensitive gas sensors for volatile organic compounds detection, Nanoscale 3 (2011) 1646–1652.
[70] R. Yoo, S. Yoo, D. Lee, J. Kim, S. Cho, W. Lee, Highly selective detection of dimethyl methylphosphonate (DMMP) using CuO nanoparticles/ZnO flowers heterojunction, Sens. Actuators B: Chem. 240 (2017) 1099–1105.
[71] M. Tonezzer, Selective gas sensor based on one single SnO_2 nanowire, Sens. Actuators B: Chem. 288 (2019) 53–59.
[72] H.-J. Kim, J.-H. Lee, Highly sensitive and selective gas sensors using p-type oxide semiconductors: Overview, Sens. Actuators B: Chem. 192 (2014) 607–627.
[73] J. Jun, J.S. Lee, D.H. Shin, J. Oh, W. Kim, W. Na, et al., Fabrication of a one-dimensional tube-in-tube polypyrrole/tin oxide structure for highly sensitive DMMP sensor applications, J. Mater. Chem. A 5 (2017) 17335–17340.
[74] K.T. Alali, J. Liu, D. Moharram, Q. Liu, J. Yu, R. Chen, et al., Fabrication of electrospun Co_3O_4/CuO pp heterojunctions nanotubes functionalized with HFIP for detecting chemical nerve agent under visible light irradiation, Sens. Actuators B: Chem. 314 (2020), 128076.
[75] J. Yoo, D. Kim, H. Yang, M. Lee, S.-o Kim, H.J. Ko, et al., Olfactory receptor-based CNT-FET sensor for the detection of DMMP as a simulant of sarin, Sens. Actuators B: Chem. 354 (2022), 131188.
[76] K.H. Kim, C.S. Park, S.J. Park, J. Kim, S.E. Seo, J.E. An, et al., In-situ food spoilage monitoring using a wireless chemical receptor-conjugated graphene electronic nose, Biosens. Bioelectron. 200 (2022), 113908.
[77] N. Tayebi, V. Kollia, P.S. Singh, Metal-oxide sensor array for selective gas detection in mixtures, arXiv Prepr. arXiv 210212990 (2021).
[78] S.G. Song, S. Ha, H.J. Cho, M. Lee, D. Jung, J.-H. Han, et al., Single-walled carbon-nanotube-based chemocapacitive sensors with molecular receptors for selective detection of chemical warfare agents, ACS Appl. Nano Mater. 2 (2018) 109–117.
[79] J. van den Broek, A.T. Guntner, S.E. Pratsinis, Highly selective and rapid breath isoprene sensing enabled by activated alumina filter, ACS Sens. 3 (2018) 677–683.
[80] T. Zhou, Y. Sang, X. Wang, C. Wu, D. Zeng, C. Xie, Pore size dependent gas-sensing selectivity based on ZnO@ ZIF nanorod arrays, Sens. Actuators B: Chem. 258 (2018) 1099–1106.
[81] S.Y. Jeong, Y.K. Moon, J.K. Kim, S.W. Park, Y.K. Jo, Y.C. Kang, et al., A general solution to mitigate water poisoning of oxide chemiresistors: bilayer sensors with Tb_4O_7 overlayer, Adv. Funct. Mater. 31 (2021) 2007895.
[82] F. Qu, S. Zhang, C. Huang, X. Guo, Y. Zhu, T. Thomas, et al., Surface functionalized sensors for humidity-independent gas detection, Angew. Chem. 133 (2021) 6635–6640.
[83] W.H Organization, WHO guidelines for indoor air quality: selected pollutants: World Health Organization. Regional Office for Europe; 2010.
[84] J.H. Sun, Z.X. Geng, N. Xue, C.X. Liu, T.J. Ma, A. Mini-System, Integrated with metal-oxide-semiconductor sensor and micro-packed gas chromatographic column, Micromachines 9 (2018) 408.
[85] G. Gregis, J.B. Sanchez, I. Bezyerkhyy, G. Weber, F. Berger, V. Fierro, et al., Detection and quantification of lung cancer biomarkers by a micro-analytical device using a single metal oxide-based gas sensor, Sens. Actuat B-Chem. 255 (2018) 391–400.
[86] T.H. Tzeng, C.Y. Kuo, S.Y. Wang, P.K. Huang, Y.M. Huang, W.C. Hsieh, et al., Portable micro gas chromatography system for lung cancer associated volatile organic compound detection, Ieee J. Solid-St Circ. 51 (2016) 259–272.
[87] S. Zampolli, I. Elmi, F. Mancarella, P. Betti, E. Dalcanale, G.C. Cardinali, et al., Real-time monitoring of sub-ppb concentrations of aromatic volatiles with a MEMS-enabled miniaturized gas-chromatograph, Sens. Actuat B-Chem. 141 (2009) 322–328.
[88] A. Larin, P.C. Womble, V. Dobrokhotov, Novel highly-integrated mems based solid state detectors for analytical gas chromatography, Sens. Actuat B-Chem. 256 (2018) 1057–1068.
[89] H.B. Zhu, J.Y. She, M.L. Zhou, X.D. Fan, Rapid and sensitive detection of formaldehyde using portable 2-dimensional gas chromatography equipped with photoionization detectors, Sens. Actuat B-Chem. 283 (2019) 182–187.
[90] Y.Y. Wu, N.A. Mashayekhi, H.H. Kung, Au–metal oxide support interface as catalytic active sites, Catal. Sci. Technol. 3 (2013) 2881–2891.
[91] S. Laursen, S. Linic, Oxidation catalysis by oxide-supported Au nanostructures: the role of supports and the effect of external conditions, Phys. Rev. Lett. 97 (2006), 026101.
[92] E. del Río, S.E. Collins, A. Aguirre, X. Chen, J.J. Delgado, J.J. Calvino, et al., Reversible deactivation of a Au/$Ce_{0.62}Zr_{0.38}O_2$ catalyst in CO oxidation: a systematic study of CO_2-triggered carbonate inhibition, J. Catal. 316 (2014) 210–218.
[93] S. Bastos, S. Carabineiro, J. Órfão, M. Pereira, J. Delgado, J. Figueiredo, Total oxidation of ethyl acetate, ethanol and toluene catalyzed by exotemplated manganese and cerium oxides loaded with gold, Catal. Today 180 (2012) 148–154.
[94] D. Andreeva, P. Petrova, J. Sobczak, L. Ilieva, M. Abrashev, Gold supported on ceria and ceria–alumina promoted by molybdena for complete benzene oxidation, Appl. Catal. B: Environ. 67 (2006) 237–245.
[95] J. Zhang, Y. Jin, C. Li, Y. Shen, L. Han, Z. Hu, et al., Creation of three-dimensionally ordered macroporous Au/CeO_2 catalysts with controlled pore sizes and their enhanced catalytic performance for formaldehyde oxidation, Appl. Catal. B: Environ. 91 (2009) 11–20.

Jihyun Lee received a Bachelor's degree in Material Science and Engineering at Kookmin University in 2020. Since 2020, she is currently a Ph.D. candidate at the Department of Materials Science and Engineering in Yonsei University under the supervision of Prof. Wooyoung Lee. She is currently studying on nanostructured metal-oxide semiconductor gas sensors.

Hyegi Min earned a Ph.D. degree in Chemical Engineering at Ulsan National Institute of Science and Technology (UNIST) in 2021. He is currently a research professor in the Korea Initiative for fostering University of Research & Innovation (KIURI) institute of the Department of Materials Science and Engineering at Yonsei University. His research has focused on the low dimensional carbon nanomaterials, nanopore detection of individual ions/molecules, heterogeneous catalysis, metal-oxide-semiconductor gas sensors, and nanoelectronics.

Yong-Sahm Choe is a CEO of iSenLab Inc. specialized for R&DB of breath analyzers. He received his B.S, M.S. and Ph. D degrees from the department of metallurgical engineering of Yonsei University in 1989, 1991, 1999, respectively and worked at TYM R&D institute from 1999 to 2011 in Korea. He developed oral malodor diagnosing devices, TWIN BREASOR and TWIN BREASOR II. His research interests are a development of stand-alone gas analyzers based on a miniaturization of gas chromatography including gas sensors.

Yun-Gyu Lee received a Ph.D. degree in architectural engineering from Yonsei University in 1998. Since 1991, he has been working as a senior research fellow at the Korea Institute of Civil Engineering and Building Technology. His research interests are in architectural environments and facilities such as indoor air quality and ventilation.

Kichul Kim received a master's degree in environmental engineering from Yonsei University in 2012. Since 2016, he has been working as a senior research at the Korea Institute of Civil Engineering and Building Technology. His research interests are in improving pollutants released indoors and standard experimental procedures for pollutants.

Hyun-Sook Lee received a Ph.D. degree in Physics at POSTECH in 2008. Since 2015, she has been working as a research professor in the Department of Materials Science and Engineering at Yonsei University. Her research interests are in various materials related to high-temperature superconductors, solid-state hydrogen storages, rare-earth/rare-earth-free permanent magnets, nanostructured metal-oxide-semiconductor gas sensors, and Pd-based hydrogen sensors.

Wooyoung Lee is the Underwood distinguished professor of the Department of Materials Science and Engineering at Yonsei University in Korea. He is also the Director of the Center for Super Critical Material Industrial Technology, National Core Materials Research Center and the institute of Korea Initiative for Fostering University of Research and Innovation. He is the President of The Korean Magnetics Society and a regular member of the National Academy of Engineering of Korea. In recent years, his research interests have centered on hydrogen sensors, various metal oxide semiconducting gas sensors, and breath analyzers. He is also studying rare-earth permanent magnets and thermoelectric materials and devices. He has received a number of awards in nano-related research areas including a Prime Minister Award (2023) in Nano Korea 2023, SeAH-Haiam Fellowship Award (2018) in The Korean Institute of Metals and Materials and a Service Merit Medal (2008) from the Government of Korea due to his contribution to the development of intellectual properties. He has authored and co-authored over 280 publications and has edited three special books on nanostructured materials and devices.